Climate Dynamics (2025) 63:85
https://doi.org/10.1007/s00382-024-07573-9

ORIGINAL ARTICLE

Estimating the decadal-scale climate predictability limit using nonlinear local Lyapunov exponent with optimal local dynamic analogues

Ruize Li[1] · Jianping Li[1,2] · Zhaolu Hou[1] · Ruipeng Sun[1] · Shixin Zhen[1] · Houbin Song[1]

Received: 23 October 2024 / Accepted: 26 December 2024

Abstract
Accurately estimating decadal predictability limits (PLs) is essential for advancing long-term climate predictions and understanding decadal-scale variability. This study combines the optimal local dynamic analog (OLDA) algorithm with the nonlinear local Lyapunov exponent (NLLE) method to estimate decadal PLs of oceanic and atmospheric variables, using long-term reanalysis datasets. Results demonstrate that the OLDA algorithm can enhance identification of analog states and improve PL estimation. The decadal PLs of sea surface temperature (SST) show regional and seasonal differences, with zonal mean values ranging from 8 to 17 years, and higher values in boreal summer and autumn, especially in the Northern Hemisphere and Southern Ocean. Sea level pressure (SLP) decadal PLs range from 8 to 11 years, exhibiting patchy distribution and seasonal variation. The global mean PL of SLP reaches about 10 years in boreal spring and 9 years in other seasons. SLP and SST PL distributions differ across seasons, reflecting the complexity of ocean–atmosphere interactions. Decadal PLs of major climate modes were also estimated, e.g., decadal PL of the SST Inter-Hemispheric Dipole (SSTID) is ~ 17 years, Atlantic Multidecadal Oscillation (AMO) ~ 14 years, Pacific Decadal Oscillation (PDO) ~ 13 years, North Atlantic Oscillation (NAO) ~ 16 years, Northern Hemisphere Annular Mode (NAM) ~ 11 years, and Southern Hemisphere Annular Mode (SAM) ~ 15 years. These modes display distinct predictability patterns and seasonal variations, highlighting their unique roles in regional climate dynamics. These findings enhance our understanding of decadal-scale predictability.

Keywords Decadal-scale predictability limit · Nonlinear local Lyapunov exponent (NLLE) · Optimal local dynamic analog (OLDA)

1 Introduction

With the development of coupled Earth system models, seamless prediction and climate forecasts have drawn more attention, with a key challenge being how to extend predictive capability beyond the subseasonal to decadal timescales and provide reliable decadal climate predictions. (Meehl et al. 2014, 2021; Boer et al. 2016; Choi and Son 2022). Decadal variability and changes within the climate system significantly affect key phenomena such as the North Atlantic Oscillation (NAO), El Niño-Southern Oscillation (ENSO), and Pacific Walker circulation, while also exerting profound socioeconomic impacts on extreme weather events, agricultural productivity, water resources, and other areas (Lin et al. 2018; Wu et al. 2021; Li et al. 2022). In long-term climate prediction, an accurate estimation of decadal-scale predictability limits (PLs), is essential for the enhancement of the accuracy of decadal climate forecasts (Kushnir et al. 2019).

Previous studies mainly assess decadal predictability through the signal-to-noise ratio or perfect model experiments (Griffies and Bryan 1997; Boer 2000, 2004, 2011; Collins 2002; Collins and Sinha 2003; Pohlmann et al. 2004; Meehl et al. 2014; Boer et al. 2016; Athanasiadis et al. 2020;

✉ Jianping Li
ljp@ouc.edu.cn

[1] Frontiers Science Center for Deep Ocean Multi-Spheres and Earth System (DOMES)/Key Laboratory of Physical Oceanography/Academy of Future Ocean/College of Oceanic and Atmospheric Sciences/Center for Ocean Carbon Neutrality, Ocean University of China, Qingdao 266100, China

[2] Laboratory for Ocean Dynamics and Climate, Qingdao Marine Science and Technology Center, Qingdao 266237, China

Published online: 13 January 2025

Zhang et al. 2021; Yeager et al. 2023; Düsterhus and Brune 2024). These studies have demonstrated that regions such as the North Atlantic Ocean, Southern Ocean, North Pacific, and tropical Pacific possess decadal-scale predictability to various degrees (Latif et al. 2006; Boer and Lambert 2008; Doblas-Reyes et al. 2013; Ho et al. 2013), with the North Atlantic and Southern Ocean being especially prominent (Boer 2000; Collins and Sinha 2003; Pohlmann et al. 2004). While the predictability of decadal sea surface temperature (SST) modes, such as the Pacific Decadal Oscillation (PDO) and Atlantic Multidecadal Oscillation (AMO), has been reasonably well-captured in some studies, there remain significant challenges to accurately simulate decadal variability (Kim et al. 2012; Sheffield et al. 2013; Meehl et al. 2014).

Despite these advancements, several challenges persist. One significant issue is the reliance on climate models (Latif et al. 2006), which are constrained by uncertainties in initial conditions and model parameters. As noted in the Intergovernmental Panel on Climate Change (IPCC) Sixth Assessment Report (AR6), these limitations may skew PL estimates, resulting in discrepancies between model-based projections and the actual predictability inherent in the climate system (Lee et al. 2021). Ding et al. (2016) applied the nonlinear local Lyapunov exponent (NLLE) method to make preliminary estimates of PLs from reanalysis data on decadal scales. This method, based on observational data, has been used to study the predictability of atmospheric and oceanic systems (Chen et al. 2006; Ding and Li 2007, 2011; Ding et al. 2010; Li and Ding 2013; Li et al. 2013; Ma et al. 2021; Hou et al. 2022, 2024). The NLLE method quantitatively determines the PLs of the atmosphere and oceans across different timescales through the analysis of the evolutionary of distances between local dynamic analogs (LDAs) within observed time series (Ding and Li 2011).

Furthermore, the traditional LDA algorithm used in the NLLE method for quantitatively determining PLs may identify false analogs when employing an unsuitable, fixed evolutionary window (EW), which necessitates further refinement and optimization (Huai et al. 2017; Ma et al. 2021). In addition, although considerable research has been conducted on decadal predictability, quantitative investigations specifically targeting decadal PLs remain insufficient. This highlights the urgent need for more systematic and quantitative assessments of decadal PLs within the climate system.

To address these challenges, this study builds upon refinements to the LDA algorithm and employs the NLLE method to investigate the spatial distribution and seasonal differences in the decadal PLs of key variables in the climate system, specifically SST and sea level pressure (SLP). The improvements to the LDA algorithm aim to mitigate the issue of false analog identification and provide more accurate estimates of decadal PLs in regions with relatively high predictability. Furthermore, this study examines key climate modes associated with SST and SLP variability. For SST, the AMO and PDO function as decadal SST modes at the basin scale, while the SST Inter-Hemispheric Dipole (SSTID) represents the global scale, and they collectively exert a significant influence on regional climate factors, including temperature, precipitation, storm tracks, and changes in ocean fronts (Zhang et al. 1997; Mantua et al. 1997; Enfield et al. 2001; Zhang and Delworth 2006; Sun et al. 2013; Xue et al. 2018b). For the primary modes of SLP, the Northern Hemisphere Annular Mode (NAM or Arctic Oscillation, AO) and the Southern Hemisphere Annular Mode (SAM) represent hemispheric-scale SLP fluctuations occurring between the polar and mid-latitude regions in the Northern Hemisphere (NH) and Southern Hemisphere (SH), while the NAO serves as a mode of large-scale circulation in the North Atlantic Ocean region, that exhibits decadal variations and trends that significantly impact regional climate (Thompson and Wallace 1998; Gong and Wang 1999; Li and Wang 2003a, b; Nan and Li 2003; Wu et al. 2009; Feng et al. 2010; Li et al. 2022; King et al. 2023). We also employed the NLLE method to investigate the decadal PLs and seasonal differences of these primary oceanic and atmospheric variability modes, aiming to enhance our understanding of the climate system.

The remainder of this paper is organized as follows: Sect. 2 describes the data and methods used in this study. Section 3 explores the spatial distributions of PLs of SST fields and PLs of their main modes, while Sect. 4 investigates the corresponding PLs of SLP fields and their main modes. Section 5 showcases the results of seasonal difference analyses of PLs of SST fields, SLP fields and major climate modes using the NLLE method. Finally, Sect. 6 presents the conclusions and discusses the major findings.

2 Data and method

2.1 Datasets

This study estimates decadal PL using over a century of reanalysis gridded data, including the monthly SST fields from the Extended Reconstructed SST version 5 (ERSST.v5) provided by the National Oceanic and Atmospheric Administration (NOAA), with a spatial resolution of 2°×2° (Huang et al. 2017), covering the period January 1854 to December 2023, and the monthly SLP fields from the Hadley Centre SLP dataset (HadSLP2r) provided by the Hadley Centre, with a spatial resolution of 5°×5° (Allan and Ansell 2006), covering the period January 1850–December 2019.

Before estimating PL, the climatological mean annual cycle and the global warming trend were removed from the monthly data at each grid point, leaving the anomalies. The decadal component of these anomalies was extracted using

a 9-year low-pass Gaussian filter. The global warming trend time series was derived from the NOAAGlobalTemp Version 6 dataset provided by the NOAA (Zhang et al. 2019a; Huang et al. 2020, 2022; Vose et al. 2021), covering the period from January 1850 to December 2023. Anomalies were calculated relative to the 1901–2000 average, based on the NOAA global warming trend time series.

The monthly time series of the AMO index, spanning January 1856–December 2022, is sourced from the Physical Sciences Laboratory (PSL) of NOAA (Enfield et al. 2001). The PDO index, defined as the leading pattern (Empirical orthogonal function, EOF) of monthly SST anomalies in the North Pacific basin north of 20°N (Zhang et al. 1997; Mantua et al. 1997), and the SSTID index, defined as the difference between hemispheric-mean SST anomalies in the NH and SH (Sun et al. 2013; Xue et al. 2018b; An et al. 2024), were both derived from the ERSST.v5 dataset for January 1854 to December 2023. The NAM and NAO indices, defined as the difference in normalized zonal-mean SLP between 35°N and 65°N (Li and Wang 2003a), and as the difference in normalized SLP regionally zonal-averaged over the North Atlantic sector (80°W–30°E) between 35°N and 65°N (Li and Wang 2003b), respectively, were derived from the HadSLP2r dataset for January 1850–December 2019. The monthly SAM index, covering January 1850–December 2015, is also sourced from PSL of NOAA (Gong and Wang 1999). Similar to the monthly gridded data, these indices have also been subjected to the 9-year low-pass Gaussian filter.

These data were used to quantitatively estimate decadal PLs. Table 1 summarizes the datasets mentioned above.

2.2 Optimal local dynamic analog (OLDA) algorithm

The NLLE (Chen et al. 2006; Ding and Li 2007) provides the theoretical basis for estimating the PL by quantifying the growth of initial errors in nonlinear dynamical systems. Estimating the PL with NLLE involves identifying dynamic analog states, which enables the analysis of the relative growth of initial error (RGIE) in relation to a reference state. The LDA algorithm, introduced by Li and Ding (2011), identifies analog states by evaluating both the initial distance between the reference state and the analog state and the evolutionary distance after a EW τ. It employs the NLLE to estimate the PL of a dynamical system based on observational or experimental data when the system's evolution equations are unknown or incomplete. A brief description of the algorithm is provided in Li and Ding (2011). The selection of an appropriate EW is critical for identifying reliable LDAs and obtaining accurate PL estimates. Huai et al. (2017) demonstrated that an unsuitable EW could result in the identification of false analog states, leading to inaccurate PL estimates. They proposed an optimal EW (OEW) using the Lorenz63 system, defining it as the time when the system's autocorrelation decays to zero. While this approach provides theoretical guidance, it is impractical for decadal PL estimation because the autocorrelation decay time for ocean–atmosphere variables may exceed the decadal PL itself. Thus, for decadal-scale studies, the EW should generally be shorter than the PL to reduce bias, necessitating new methods for selecting an appropriate EW. Ma et al. (2021) pointed out that there are many potential analog states for the reference state, and there exists an OLDA state that provides the longest PL. However, determining the OLDA requires evaluating all potential analog states in the dataset, a process that is computationally expensive and constrained by the finite length of observational data, limiting its practical application. To address these challenges, this study introduces a novel approach to dynamically select EWs and identify analog states. By leveraging the continuous analog of the reference state, this method avoids the need to evaluate all potential analogs, reducing computational costs and enabling efficient use of limited datasets. Furthermore, to ensure robust PL estimates, we employ an OLDA ensemble ($OLDA_E$) average, which integrates multiple high-quality analog states rather than relying on a single OLDA.

In the traditional LDA algorithm, the initial distance is calculated as the distance in phase space between the reference state and all potential analog states, identified by traversing the dataset to identify the closest spatial matches.

Table 1 Datas utilized in this study

Data	Source	Resolution	Period
ERSST.v5	National Oceanic and Atmospheric Administration (NOAA)	2°×2°	1854–2023
HadSLP2r	UK Met Office Hadley Centre	5°×5°	1850–2019
AMO index	NOAA	/	1856–2022
PDO index	Zhang et al. 1997; Mantua et al. 1997	/	1854–2023
SSTID index	Sun et al. 2013; Xue et al. 2018a, b, c	/	1854–2023
NAM index	Li and Wang 2003a	/	1850–2019
NAO index	Li and Wang 2003b	/	1850–2019
SAM index	NOAA	/	1850–2015

However, previous studies have not discussed whether this initial distance might be excessively large for different EWs (Li and Ding 2011; Huai et al. 2017; Ma et al. 2021). Furthermore, this traversal process significantly increases computational costs, particularly for large datasets. For any initial state $x(i)$ of one-dimensional variable x [e. g. the time series is given by $\{x(i), i \in K = 1,2,...,N\}$], the neighborhood of all initial distances can be visualized as a circle centered at $x(i)$ with radius r in the phase space. This circle includes initial distances of different magnitudes and directions from $x(i)$. Therefore, it is possible to select false LDA states with an initial distance $d_i > r$ if the evolutionary distance d_e is relatively small within τ. It is necessary to consider the overall distribution of initial distances for variable x and, within the radius r, combine this with a continuous, dynamic EW τ to identify the OLDA states. We propose the following method to progressively identify OLDA:

First, determine the initial distance radius r to avoid an excessively large initial distance between the reference state $x(i)$ and the analog state $x(j)$ during the identification of the OLDA. Since the neighborhood of the initial distance should be sufficiently small, it is first necessary to discuss the possible minimum distance between any state in the time series and all other states. For a one-dimensional observed variable $\{x(i), i \in K = 1,2,...,N\}$, where N represents the time series length, for any $i \in [1, K]$, we have:

$$\delta_{i,j} = |x(i) - x(j)|, \tag{1}$$

$$\delta_i = \left\{\delta_{i,j}, (j \in [1, K], i \neq j)\right\}. \tag{2}$$

where δ_i represents the distance between any point in the series and all other points. Let $\delta = \left\{\delta_{imin}, i \in [1, K]\right\}$, where δ denotes the possible minimum distance between any point in the series and all other points. To ensure that each point has sufficient neighbors within the initial distance radius, let $\delta_{max} = \max(\delta)$. Estimate the initial distance radius r as $d^* = m \times \delta_{max}$, where $m \in N^+$. In this study, we set $m = 2$ to avoid an to avoid an excessively small radius and ensure an adequate number of initial analog states, which helps prevent potential issues in subsequent steps while also reducing computational costs.

Secondly, determine the initial state set based on the estimated initial distance radius d^*. For the variable x, let $\boldsymbol{A}_0(i) = \left\{j, \delta_{i,j} \le d^*\right\}$. Then, $x\left(\boldsymbol{A}_0(i), i\right) = \left\{x(j), j \in \boldsymbol{A}_0(i)\right\}$ represents the initial set of states analog to $x(i)$ at time $\tau_0 = 0$. The number of elements in $\boldsymbol{A}_0$ is denoted as m_0, and the corresponding initial distances are given by $d_i\left(\boldsymbol{A}_0(i), i\right) = \left\{\delta_{i,j}, j \in \boldsymbol{A}_0(i)\right\}$.

Thirdly, estimate the preliminary PL (T_{p0}). Using the initial state set, apply the LDA algorithm in combination with the NLLE method (Li and Ding 2011) to calculate T_{p0}. In the traditional LDA algorithm, the EW is determined by the time at which the autocorrelation decreases to a certain threshold value. Here, T_{p0} serves as a preliminary estimate, providing a foundation for determining an EW that captures the system's intrinsic dynamical characteristics.

Fourth, identify the set of OLDA. For the variable x, the initial distance d_i between the reference state $x(i)$ and the analog state $x(l) \in x\left(\boldsymbol{A}_0(0), 0\right)$ (where $\left|t_0 - t_j\right| > D$, where D is the time taken for autocorrelation coefficient of the variable x to drop to around 0.0, ensuring that the influence of the persistence of $x(i)$ is avoided) is given by:

$$d_i = |x(i) - x(l)|, \left(d_i \in d_i\left(\boldsymbol{A}_0(0), 0\right)\right). \tag{3}$$

Introduce $\tau_L = c_L T_{p0}\left(c_L \in R^+, L = 1, 2, \ldots, p\right)$ as the local EW. The evolutionary distance can then be expressed as:

$$d_e = \frac{1}{t+1} \sum_{i=0}^{t} \left|x\left(i + \tau_L\right) - x\left(l + \tau_L\right)\right|, \tag{4}$$

where t is the ratio of τ_L to the sampling interval. The total distance is denoted as d_t, where $d_t = d_i + d_e$. By traversing all eligible states in the time series, the $m_i (i = 1, 2, \ldots, k)$ states with the smallest d_t are identified as the LDA ensemble $\boldsymbol{A_i}$ (where $\boldsymbol{A_i} \subseteq \boldsymbol{A}_{i-1}$). Replacing $\boldsymbol{A}_{i-1}$ with $\boldsymbol{A_i}$ and τ_{L-1} with τ_L, this process is repeated multiple times to obtain $\boldsymbol{A}_{i+1}$ (with $m_{i+1} \le m_i$). By sorting d_t in ascending order, the smallest m_p state points form the analog state set $\boldsymbol{A}_{i+1}$, known as the $\mathrm{OLDA_E}$. The analog states are denoted as $x\left(I_k\right)$. Let $m_k = 1$, the state with the smallest d_t is identified as the OLDA state, denoted as $x(l)$. Where $l, I_k \in K$ and $l, I_k \neq i$, with $k = 1, 2, 3, \ldots, m_p$. Based on the OLDA algorithm, $\mathrm{OLDA_E}$ can appropriately expand the sample of analogous states and optimize the estimation of the PL in the case of limited observational data. The detailed parameters of the OLDA and $\mathrm{OLDA_E}$ algorithm used in this study are shown in "Appendix A".

To compare the error growth between reference states and analog states obtained from LDA, OLDA, and $\mathrm{OLDA_E}$ algorithms, we introduced the Lorenz63 system (Lorenz 1963) and employs the NLLE method to quantitatively estimate its PLs. The Lorenz63 model is:

$$\begin{cases} \dot{x} = -\sigma(x - y) \\ \dot{y} = -xz + rx - y \\ \dot{z} = xy - bz \end{cases}, \tag{5}$$

where $\sigma = 10$, $r = 28$, $b = 8/3$. The time series of the variables x, y, and z is obtained with the fourth-order Runge–Kutta method, a time step of $\Delta = 0.01$. The time series includes 1×10^6 points.

Figure 1 shows the mean absolute error growth and RGIE curves for x, y, and z variables of the Lorenz63

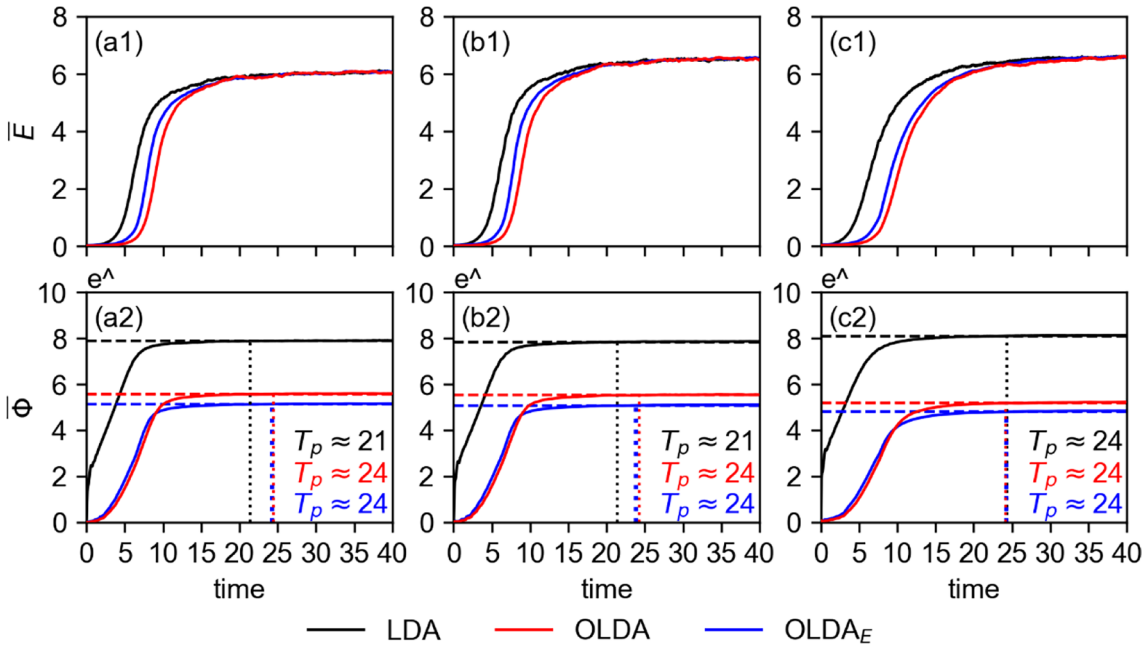

Fig. 1 **a1** Mean absolute error ($\overline{E}$) growth of the variable x of the Lorenz63 model estimated by the LDA (black line), OLDA (red line), and $OLDA_E$ (blue line) algorithms, respectively. **b1**, **c1** are the same as **a1**, but for the variables y and z of the Lorenz63 model, respectively. **a2**, **b2**, **c2** As in **a1**, **b1**, **c1**, but for mean relative growth of initial error (RGIE, $\overline{\Phi}$), respectively. The dashed horizontal lines represent the 99% levels of the saturation values from the three algorithms, respectively, and the dotted vertical lines represent the corresponding predictability limits (T_p), respectively

system obtained using different algorithms, along with their PLs. The mean absolute error growth curves for the x, y, and z variables converge to the same saturation level across all algorithms; however, during the error growth phase, the OLDA algorithm shows a significantly lower error rate increase compared to the LDA algorithm, particularly within the first 5 dimensionless time units (DTUs) of the linear error growth stage (Fig. 1a1–c1). Similarly, the RGIE rates from the OLDA algorithm are obviously lower in the initial stages compared to the LDA algorithm, with the PLs of the x and y variables improving from 21 to 24 DTUs, while the z variable's PL remains at 24 DTUs with all algorithms, though the RGIE curve also shows noticeable improvement (Fig. 1a2–c2). The comparison of error growth characteristics clearly highlights the improvements offered by the OLDA algorithm over the LDA algorithm. Moreover, the OLDA algorithm initially filters out state points outside the initial distance radius, which significantly reduces computation time. In this study, the PL is estimated by identifying the time at which the RGIE reaches 99% of its saturation level (Li and Ding 2011). These comparison results substantiate the effectiveness of the OLDA algorithm in ameliorating the mean absolute error growth and RGIE based on the experimental data of a single variable of the Lorenz63 system.

3 Decadal PL of monthly SST

3.1 Spatial distribution of decadal PL of SST

Figure 2a shows the spatial distribution of the PL of 9-year low-pass filtered SST based on the ERSST.v5 dataset, with the OLDA algorithm applied to the NLLE method. The zonal mean result indicates that the decadal PL of SST ranges from about 8–17 years, with a global mean of about 10 years. Regions with high decadal PLs are mainly found in the NH 15° – 45°N, with PL values of about 11–12 years, and in the SH 30° – 60°S, with PL values of about 11–14 years. In contrast, lower PLs are observed in the low to mid-latitude SH (0° – 40°S), with values of about 8–10 years. The zonal mean PL reaches about 17 years in the 60° – 72°N region, influenced by local PL in the Norwegian Sea in the North Atlantic (60° – 72°N, 0° – 20°E), which is less representative. These results align with previous study (Ding et al. 2016), but the LDA algorithm estimates a lower SST decadal zonal mean (about 6–9 years) compared to OLDA, highlighting the OLDA's advantage.

The decadal PL of SST exhibits significant spatial variations across ocean basins (Fig. 2a). Notable decadal PL is observed in the northern Pacific Ocean, northern Atlantic Ocean, tropical Indian Ocean, and Southern Ocean, consistent with the findings of Ding et al. (2016), although

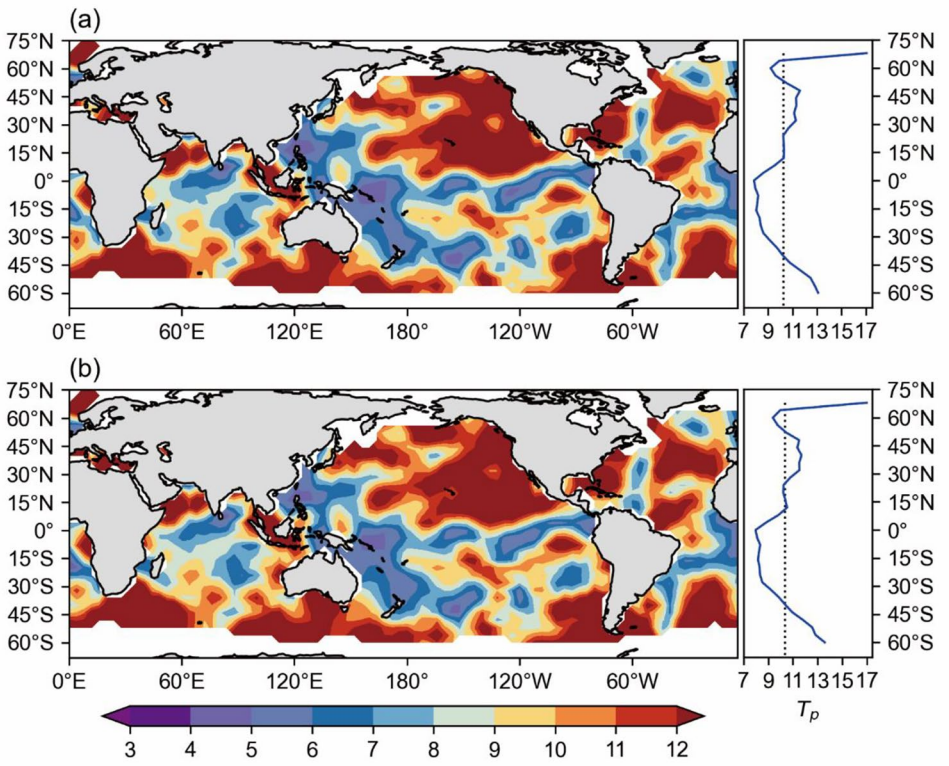

Fig. 2 **a** Spatial distribution (left) of the SST predictability limit (T_p, in years) estimated by the OLDA algorithm for the 9-year low-pass filtered ERSST. v5 dataset, and its zonal mean profile (blue solid line) on the right, with the global mean (black dashed line). **b** As in **a**, but for the $OLDA_E$ algorithm

spatial patterns differ. The eastern North Pacific Ocean (5° – 60°N, 155°E – 100°W) also presents extensive high PL (over 9 years), which was not detected by previous study (Ding et al. 2016). Decadal PL in the low- to mid-latitude South Pacific is generally low, with a clear asymmetry between the hemispheres. The North Atlantic Ocean (0° – 60°N, 95° – 5°W) shows high decadal PLs (about 7–12 years) with distinct regional characteristics. Although tropical SSTs generally have lower decadal predictability, the tropical North Atlantic Ocean (0° – 20°N, 55° – 20°W), Arabian Sea (0° – 20°N, 45° – 80°E), and Maritime Continent (10°S – 10°N, 90° – 130°E) have higher PLs (about 8 – 12 years). The Southern Ocean (30° – 65°S, 0° – 360°E) generally shows high predictability, forming a zonal band with a PL exceeding 12 years. However, some regions exhibit lower PLs. Similar to Ding et al. (2016), the central-eastern equatorial Pacific (10°N – 10°S, 140° – 60°W) shows a lower decadal PL (about 4 – 7 years), likely primarily influenced by the interannual variability of ENSO. Additionally, our estimates indicate that the western North Pacific Ocean (10° – 30°N, 110° – 140°E) has a decadal PL of less than 7 years, lower than that in the previous study (Ding et al. 2016), possibly due to data version differences or inherent limitations affecting SST decadal variability representation in these regions.

Previous studies have extensively examined the decadal variability of SST in the North Pacific Ocean and North Atlantic Ocean, with a focus on phenomena such as the PDO and AMO (Mantua et al. 1997; Power et al. 1999; Kerr 2000; Enfield et al. 2001; Trenberth and Shea 2006; Zhang and Delworth 2006; Newman et al. 2016; Deser and Phillips 2021). The spatial distribution of the SST decadal PL (Fig. 2) reveals a high-value region in the eastern North Pacific Ocean (5° – 60°N, 155°E – 100°W), where PL is notably concentrated. Bond et al. (2003) emphasized that North Pacific Ocean SST decadal predictability is primarily driven by internal decadal variations and that a single indicator, such as the PDO, is insufficient to fully characterize the climate. North Pacific Ocean decadal variability is also influenced by other modes and ocean currents, such as the North Pacific Gyre Oscillation (NPGO), the Kuroshio-Oyashio Extension (KOE), among others (Qiu 2003; Di Lorenzo et al. 2008; Liu and Di Lorenzo 2018; Joh et al. 2022; Lorenzo et al. 2023). The presence of multiple SST decadal variability modes in the eastern North Pacific Ocean creates favorable conditions for the region's high decadal predictability.

In the North Atlantic basin, similar high PL regions exist, likely due to the AMO and the Atlantic Meridional Overturning Circulation/thermohaline circulation (AMOC/THC, Levine et al. 2017; Yeager and Robson 2017; Zhang et al. 2019b; Yeager 2020). The decadal variability of the tropical

Atlantic, as suggested by early studies (Carton et al. 1996; Rajagopalan et al. 1998) and reinforced by Nnamchi et al. (2023), is positively influenced by Atlantic Ocean circulation. Although the SH has a larger ocean area, the key PL regions are concentrated in the Southern Ocean (30° – 65°S, 0° – 360°E), possibly due to sparse SST observations. Xue et al. (2018a) identified the South Atlantic multi-decadal variability (SAMV), which affects South Indian Ocean SST variability through atmospheric circulation (Xue et al. 2018c). However, research on Southern Ocean decadal variability remains limited and warrants further exploration.

In the tropics, the decadal PL of the Arabian Sea (0° – 20°N, 45° – 80°E) may be linked to the Indian Ocean Dipole (IOD) influenced by ENSO and PDO (Han et al. 2014; Krishnamurthy and Krishnamurthy 2016), the decadal IOD (Dong and McPhaden 2017), the Interdecadal Pacific Oscillation (IPO, Dong et al. 2016a, b), and the NAO (Xie et al. 2021). The SST decadal variability in the Maritime Continent (10°S – 10°N, 90° – 130°E), at the junction of the Indian and Pacific Ocean basins, may be affected by the Indonesian Throughflow (ITF) and influence East Asian climate through the decadal Pacific–Japan (PJ) pattern (Zhang et al. 2018; Li et al. 2018; Xie et al. 2022). Moreover, the decadal PL of SST is influenced not only by internal variability but also by inter-basin interactions. For instance, the tropical Atlantic Ocean may impact Pacific Ocean decadal climate (Chikamoto et al. 2016), and the North Atlantic Ocean is a significant contributor to Pacific decadal variability (Yao et al. 2021). These interactions require further investigation.

Figure 2b shows the spatial distribution of the decadal PL of SST estimated using the $OLDA_E$ algorithm. While maintaining consistency with the spatial patterns observed in Fig. 2a, the expansion of the sample size during calculations has resulted in higher decadal PLs in certain regions, such as the eastern North Pacific Ocean (5° – 60°N, 155°E – 100°W). This indicates that the $OLDA_E$ algorithm not only robustly reproduces the OLDA results but also provides better estimates of the potential decadal PL under conditions of limited data length.

3.2 RGIE characteristics and decadal PLs of key SST regions

Figure 2 reveals several key regions with relatively high SST decadal PLs, despite variations across ocean basins. Based on this, we averaged the time series of grids in regions where the decadal PLs exceed 10 years and estimated the decadal PLs of these areas. These estimates are illustrated in Fig. 3, which shows the regionally averaged RGIE for SST in key areas including the eastern North Pacific Ocean (5°N – 60°N, 155°E – 100°W, Fig. 3a), the Gulf Stream region (15° – 45°N, 95° – 60°W, Fig. 3b), mid-latitude North Atlantic Ocean (25° – 60°N, 55° – 5°W, Fig. 3c), tropical North Atlantic Ocean (0° – 20°N, 55° – 20°W, Fig. 3d), the Arabian Sea (0° – 25°N, 45° – 80°E, Fig. 3e), Maritime Continent (10°S – 10°N, 90° – 130°E, Fig. 3f), eastern

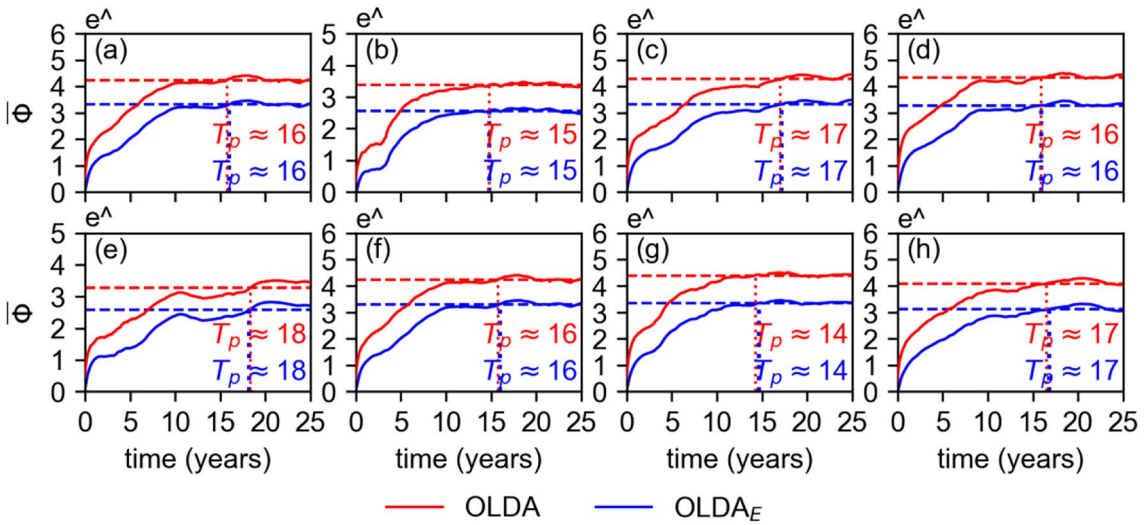

Fig. 3 RGIE and predictability limit of the 9-year low-pass filtered monthly ERSST obtained using the OLDA (red line) and $OLDA_E$ (blue line) of the NLLE method for different ocean basins. **a** eastern North Pacific Ocean (5°N – 60°N, 155°E – 100°W), **b** the Gulf Stream (15° – 45°N, 95° – 60°W), **c** mid-latitude North Atlantic Ocean (25° – 60°N, 55° – 5°W), **d** tropical North Atlantic Ocean (0° – 20°N, 55° – 20°W), **e** the Arabian Sea (0° – 25°N, 45° – 80°E), **f** the Maritime Continent (10°S – 10°N, 90° – 130°E), **g** eastern South Pacific Ocean (5° – 30°S, 150° – 70°W) and **h** Southern Ocean (30° – 65°S, 0° – 360°E). The dashed horizontal lines represent the 99% levels of the saturation values from the two algorithms, respectively, and the dotted vertical lines represent the corresponding predictability limits (T_p, in years), respectively

South Pacific Ocean (5° – 30°S, 150° – 70°W, Fig. 3g) and the Southern Ocean (30° – 65°S, 0° – 360°E, Fig. 3h). It is evident that the initial error growth rates vary across different ocean basins, leading to differences in the estimated decadal PLs, with SST decadal PLs in these key regions all over 14 years.

Quantitative estimates clearly indicate that the North Pacific and North Atlantic basins have relatively high decadal PLs, consistent with previous research showing significant decadal variability in SST within these regions. Similarly, the Arabian Sea (Fig. 3e) and the Southern Ocean (Fig. 3h) also exhibit high decadal PLs, consistent with earlier quantitative estimates (Ding et al. 2016). Nevertheless, further comprehensive exploration is needed to understand the mechanisms driving SST decadal variability in these basins and its broader implications.

3.3 Decadal PLs of major SST modes

In addition to the key regions of SST decadal PLs, we used the OLDA and $OLDA_E$ algorithms along with NLLE to estimate the major decadal modes of SST, including AMO, PDO, and SSTID. Figure 4 presents the RGIE and decadal PLs of these indices after the 9-year low-pass Gaussian filter. The RGIE for each mode reveals distinct growth patterns: The AMO index shows rapid initial error growth for the first 10 years, which then slows and eventually saturates, with a decadal PL of about 14 years (Fig. 4a). The PDO index exhibits rapid error increase in the first 7 years, followed by a deceleration and eventual saturation, with a decadal PL of about 13 years (Fig. 4b). For the SSTID index, initial error grows rapidly over the first 13 years, then slows and stabilizes, which results in a decadal PL of approximately 17 years (Fig. 4c). These results indicate that the PLs of different decadal SST modes respond differently to initial conditions.

Previous studies suggest that initial conditions can provide predictability during the rapid error growth phase but may later be influenced by nonlinear processes such as internal variability or external forcing (Ding et al. 2010, 2011, 2016; Ding and Li 2011; Li and Ding 2013). Consequently, in addition to internal SST variability, factors such as THC, sunspot activity cycles, and volcanic activity may also impact the decadal PLs of these modes. Among the major decadal modes of SST, SSTID exhibits the longest PL, extending to 17 years, which is greater than that of AMO and PDO. As a global-scale mode, SSTID's interhemispheric asymmetric temperature variability is independent of regional SST modes. In contrast, the PDO and AMO serve as regional manifestations of SSTID, reflecting temperature variability specifically in the North Pacific and North Atlantic, respectively (Sun et al. 2013; Xue et al. 2018b). The higher decadal PL of AMO, regulated by the predictable AMOC (Msadek et al. 2010), aligns with Ding et al. (2016), while the PDO's slightly lower PL reflects its dependence on wind-driven upper-ocean circulation in the North Pacific (Liu and Di Lorenzo 2018).

4 Decadal PL of monthly SLP

4.1 Spatial distribution of decadal PL of SLP

The decadal predictability of SLP is crucial for understanding and improving climate predictions. In this study, we estimated the decadal PLs of SLP using the OLDA and $OLDA_E$ algorithms combined with the NLLE method (Fig. 5). Consistent with the quantitative estimates of SST decadal PLs (Fig. 2), the $OLDA_E$ algorithm accurately reproduces the spatial distribution of SLP decadal PLs derived from the OLDA algorithm (Fig. 5a), while also demonstrating longer

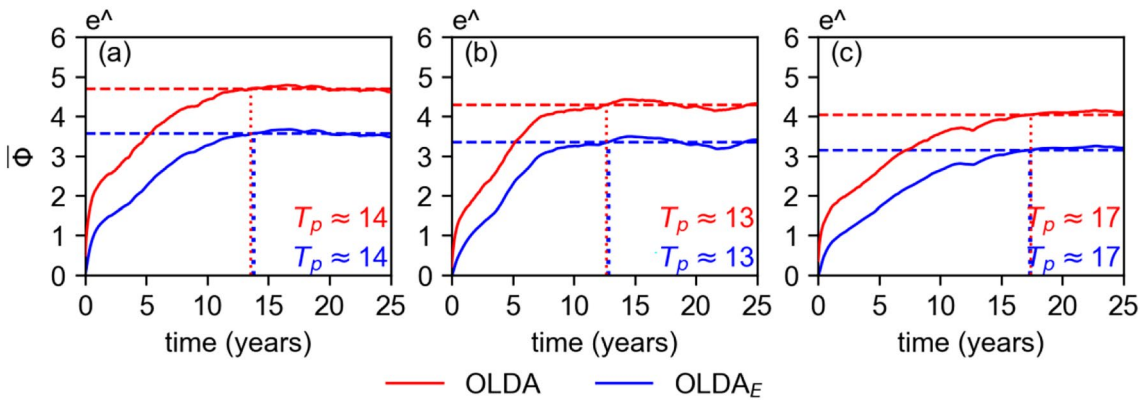

Fig. 4 **a** As in Fig. 3a, but for the AMO index. **b** As in **a**, but for the PDO index. **c** As in **a**, but for the SSTID index

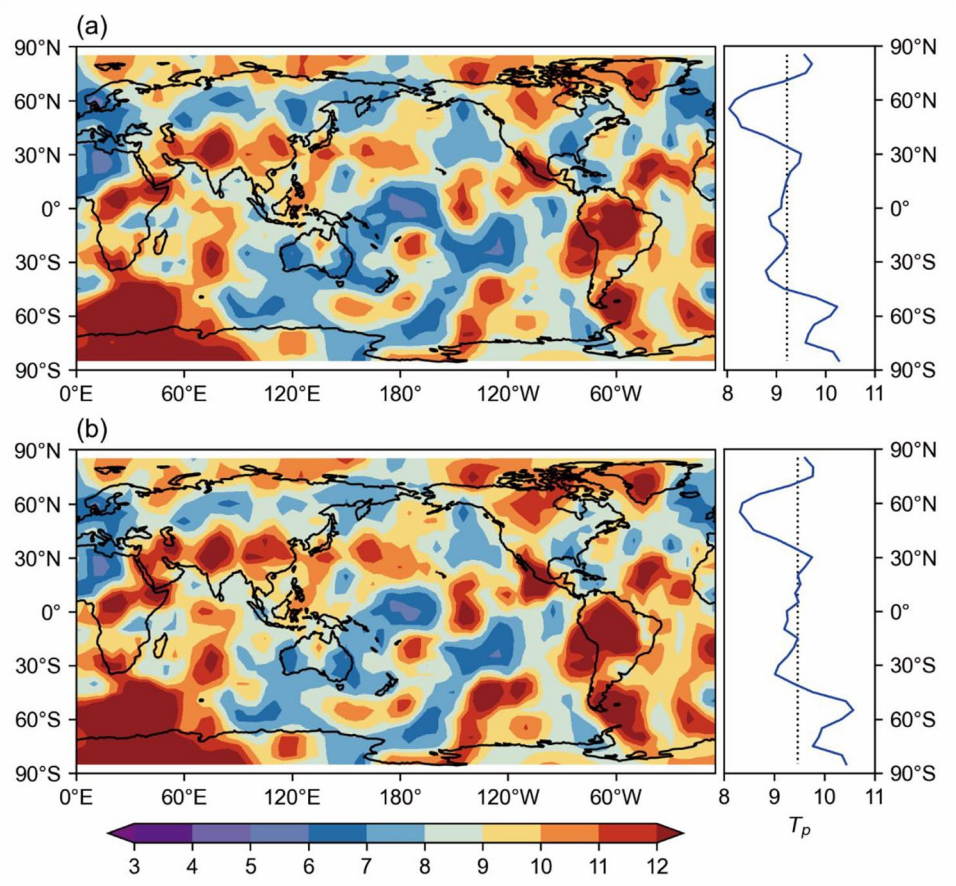

Fig. 5 As in Fig. 2, but for SLP predictability limit (T_p, in years) based on the 9-year low-pass filtered monthly HadSLP2r dataset

potential decadal PLs in certain regions (Fig. 5b), even with limited data length.

The decadal PLs of SLP, as indicated by zonal mean results (Fig. 5), are generally lower than those of SST (Fig. 2) and range from about 8 to 11 years. The SH generally exhibits higher PLs than the NH. Regions within 70° – 85°N and 15° – 30°N have limits above the global mean, while the SH mid to high latitudes (50° – 85°S) show higher PLs, possibly influenced by the decadal variability of the SAM mode and Southern Ocean SST. In contrast, the PLs of SLP in the 15°N – 40°S region are relatively low (about 9 years), a feature similar to the zonal mean of SST and possibly influenced by it. However, in the NH mid-latitude region (40° – 70°N), the decadal PL of SLP is lower than the global mean (about 8–9 years), a pattern that diverges from the zonal mean of SST (Fig. 2), which indicates the influence of other non-SST factors.

In terms of spatial distribution, although the decadal PL limit of SLP exceeds 10 years in some areas, the distribution of high-value regions is relatively scattered and mainly appears in patchy patterns (Fig. 5). Compared to SST (Fig. 2), the high-value regions for SLP are more dispersed in distribution. This reflects greater spatial heterogeneity and suggests that the decadal influencing factors for SLP are more complex than those for SST. This reflects a certain degree of spatial heterogeneity and suggests that the decadal influencing factors for SLP are more complex than those for SST. Consistent with previous quantitative estimates (Ding et al. 2016), we observed relatively high decadal PLs in the mid to high latitudes south of Africa (50° – 85°S, 0° – 80°E) and the NH high latitudes (65° – 85°N, 0° – 360°E), which may contribute to the zonal mean PL in these regions being higher than the global mean.

Across the ocean basins, we identified regions with relatively high decadal PLs of SLP (Fig. 5), including the northwest Pacific Ocean (20° – 40°N, 130° – 170°E), the central and eastern Pacific Ocean (10°S – 20°N, 155° – 110°W), the subtropical North Atlantic Ocean (10° – 30°N, 55° – 15°W), the southern Indian Ocean (15° – 40°S, 65° – 85°E), and the Southern Ocean (30° – 65°S, 0° – 360°E), where the PL exceeds 10 years. In the central and eastern Pacific Ocean, the subtropical North Atlantic Ocean, and the Southern Ocean, the decadal PLs of SLP align with relatively high decadal PLs of SST (over 10 years) (Fig. 2). This alignment may result from the influence of local SST decadal variability on SLP, which contributes to the higher decadal PLs of SLP. However, when compared to the spatial distribution of the decadal PL of SST shown in Fig. 2, the high-value

regions of SLP within each ocean basin do not fully correspond with those of SST. For instance, while the northwest Pacific Ocean and the southern Indian Ocean exhibit higher decadal PLs of SLP (over 10 years), the corresponding SST decadal PLs in these regions are lower (below 9 years). This suggests that SLP decadal predictability is not solely driven by local SST decadal variability. Further investigation is required to identify other potential sources of SLP decadal predictability. Besides the ocean basins, some continental regions also display relatively high decadal PLs (Fig. 5), such as central Africa (5°S – 15°N, 10° – 55°E), the Arabian Peninsula – East Asia (20° – 45°N, 45° – 120°E), northern North America (50° – 65°N, 120° – 85°W), and the South American continent (5°N – 35°S, 85° – 45°W). In these areas, the decadal PL of SLP generally exceeds 10 years. In contrast, in regions with high decadal PLs of SST, the SLP may not always have high decadal PLs. For instance, in the northeastern Pacific (25° – 60°N, 160° – 125°W), the decadal PL of SST exceeds 10 years (Fig. 2), while SLP is only about 6 to 7 years.

In terms of potential physical mechanisms, the mid to high latitudes south of Africa (50° – 85°S, 0° – 80°E) and the NH high latitudes (65° – 85°N, 0° – 360°E) may be influenced by the primary decadal modes in these regions: the NAO and the SAM. This influence likely contributes to the relatively high decadal PLs observed in these areas. Traditional studies suggest that atmospheric memory is typically short, with atmospheric signals primarily used for seasonal predictions (Redolat et al. 2020). However, some atmospheric signals coupled with SST also exhibit decadal variability and affect local climates (Sun et al. 2015; Li et al. 2019, 2022; Redolat et al. 2020). In the northwest Pacific (20° – 40°N, 130° – 170°E), the decadal PL of SLP may be influenced by interactions across ocean basins, such as the AMO (Sun et al. 2017). In the central and eastern tropical North Pacific (5° – 25°N, 155° – 100°W), where SST shows high decadal PLs (Fig. 2), the decadal PL of SLP might be impacted by local decadal variability in SST. The decadal PL of SLP in the subtropical North Atlantic (10° – 30°N, 55° – 15°W) could be influenced by both the high decadal PL of local SST and the NAO. In the Indian Ocean, previous research (Feng et al. 2012) has identified a coupled interaction between SST and SLP in the southern Indian Ocean, with primary manifestations as low-frequency changes. Additionally, topographic elevation may also have some influence, such as that of the Tibetan Plateau and the Congo Basin, among others.

Overall, the decadal PL of SLP in the SH mid to high latitudes (40° – 85°S, 0° – 360°E) is relatively high, potentially influenced by the high decadal PL in the Southern Ocean (30° – 65°S, 0° – 360°E) or by a combination of factors such as SAM or Antarctic Sea ice. On land, the decadal PL of SLP may be influenced by nearby oceanic decadal variability (Boer 2000), such as the area in central Africa adjacent to the Arabian Sea shown in Fig. 2, as well as land–atmosphere interactions. However, further investigation is needed to explore additional influencing mechanisms. The differing spatial distributions of SST and SLP PLs indicate that atmospheric predictability, even at lower levels, is not exclusively driven by surface conditions; rather, remote factors and internal atmospheric variability also contribute significantly. This emphasizes the limitations of single-factor predictions and highlights the need to consider nonlinear interactions among multiple factors.

4.2 RGIE characteristics and decadal PLs of key SLP regions

Figure 6 shows the regional averages of grids where the decadal PL of SLP is at least 10 years. Both the OLDA and $OLDA_E$ algorithms were used to estimate relatively high decadal PLs, with the following specific results: the decadal PL in the mid to high latitudes south of Africa (50° – 85°S, 0° – 80°E) is about 14 years (Fig. 6a), in the southeastern Pacific Ocean (40° – 75°S, 150° – 105°W) about 16 years (Fig. 6b), and in the southwestern Atlantic Ocean (45° – 60°S, 70° – 50°W) about 14 years (Fig. 6c), all of which are located in the mid to high latitudes of the SH. The relatively high decadal PLs of SLP in these regions may be related to the high decadal PLs of SST in the Southern Ocean or the influence of the SAM. The decadal PL in the NH high latitudes (65° – 85°N, 0° – 360°E) is about 10 years (Fig. 6d), possibly influenced by the NAM or sea ice.

In the region from the Arabian Peninsula-northwestern Pacific Ocean (20° – 45°N, 45°E – 170°E), the decadal PL is about 17 years (Fig. 6e), represented as multiple centers. The $OLDA_E$ algorithm illustrates the spatial distribution of these centers (Fig. 5), which may be influenced by land–atmosphere interactions. The decadal PL in the eastern North Pacific Ocean-central America (0° – 30°N, 155° – 90°W) is around 19 years ($OLDA_E$ algorithm) or 15 years (OLDA algorithm) (Fig. 6f), and this higher predictability may be related to the decadal PLs of SST in the eastern North Pacific and the North Atlantic Current. The decadal PL in the subtropical North Atlantic Ocean (10° – 30°N, 55° – 15°W) is about 14 years (Fig. 6g), likely influenced by the high SST decadal PL in this region and factors such as the NAO. The decadal PL in the southern Indian Ocean (15° – 40°S, 65° – 85°E) is around 10 years (Fig. 6h).

In central Africa (5°S – 15°N, 10° – 55°E), predominantly land-based, shows a decadal PL of about 17 years (Fig. 6i), while the land area in northern North America (50° – 65°N, 120° – 85°W) has a decadal PL of about 15 years (Fig. 6j). South America (5°N – 35°S, 85° – 45°W) stands out with a decadal PL of about 21 years (Fig. 6k), the highest of the

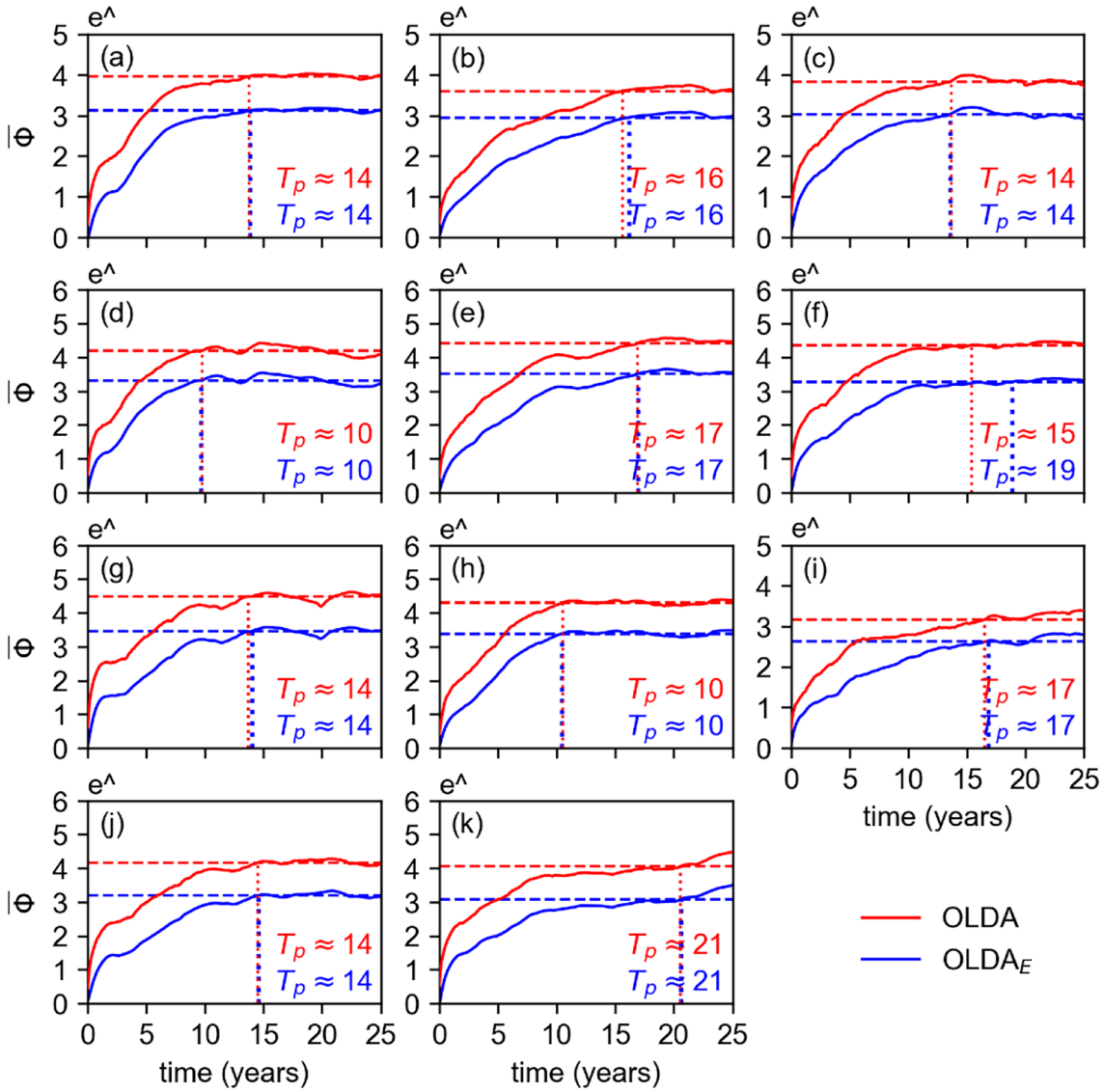

Fig. 6 As in Fig. 3, but for the 9-year low-pass filtered monthly HadSLP2r of the NLLE method for different regions. **a** mid to high latitudes south of Africa (50° – 85°S, 0° – 80°E), **b** southeastern Pacific Ocean (40° – 75°S, 150° – 105°W), **c** southwestern Atlantic Ocean (45° – 60°S, 70° – 50°W), **d** NH high latitudes (65° – 85°N, 0° – 360°E), **e** the Arabian Peninsula-northwestern Pacific Ocean (20° – 45°N, 45°E – 170°E), **f** eastern North Pacific Ocean-central America (0° – 30°N, 155° – 90°W), **g** subtropical North Atlantic Ocean (10° – 30°N, 55° – 15°W), **h** southern Indian Ocean (15° – 40°S, 65° – 85°E), **i** central Africa (5°S – 15°N, 10° – 55°E), **j** northern North America (50° – 65°N, 120° – 85°W) and **k** south America (5°N – 35°S, 85° – 45°W)

selected regions. These regions should be given particular attention in decadal SST predictions.

4.3 Decadal PLs of major SLP modes

Based on the OLDA and $OLDA_E$ algorithms, we applied the NLLE to estimate the decadal PLs of major SLP modes, which include the NAM, the SAM, and the NAO, as shown in Fig. 7. The RGIE curves for these indices reveal the following growth patterns: the NAM index demonstrates a steady increase after an initial phase of rapid growth and fluctuations during the first five years, with a decadal PL of approximately 11 years (Fig. 7a). This is significantly higher than the about 4 years estimated using the LDA algorithm (Ding et al. 2016), which potentially underestimates the decadal PLs in the Arctic region. The SAM index shows a decadal PL of about 15 years (Fig. 7b). In the SH, high-value regions of SST and SLP from subpolar to polar areas suggest that factors such as SST and sea ice play a crucial role in the determination of the decadal PL. Among the three SLP modes, the NAO index has the longest decadal PL, about 16 years (Fig. 7c).

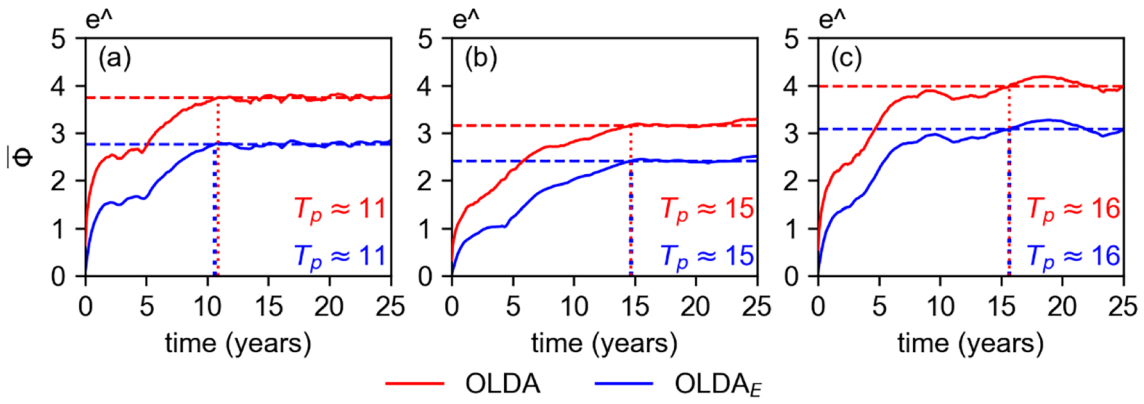

Fig. 7 **a** As in Fig. 3a, but for the NAM index. **b** As in **a**, but for the SAM index. **c** As in **a**, but for NAO index

The decadal PLs of SLP modes are influenced by various factors, like SST and sea ice variability in mid to high latitudes, as well as stratospheric conditions, quasi-biennial oscillation (QBO), and seasonal variations (Hu and Tung 2002; Smith et al. 2016; Lou et al. 2017; Feng et al. 2021). While the main SLP modes demonstrate high potential for decadal predictability, their actual limits are affected by variability across different scales and sources.

5 Seasonal differences in decadal PLs

5.1 Seasonal differences in decadal PLs of SST

Figure 8 illustrates the spatial and zonal mean distribution of seasonal mean SST decadal PLs in boreal spring (March–May, MAM), summer (June–August, JJA), autumn (September–November, SON), and winter (December-February, DJF). Quantitative estimates indicate that the global mean decadal PL of SST is about 10 years, with variations observed across different seasons (Fig. 8a, d, right panels). However, PLs are slightly higher in summer and autumn compared to spring and winter. This difference is primarily due to the lower overall PLs in spring in the SH and in the mid and lower latitudes of the SH during winter. While the zonal mean profiles of seasonal decadal PLs (Fig. 8, right panels) exhibit some similarities to the zonal mean profile of monthly SST decadal PLs (Fig. 2, right panels), significant seasonal differences are still apparent. This highlights the significant impact of seasonality on decadal PLs, particularly in the mid-to-high latitudes of both hemispheres and the tropical regions of the SH. Therefore, spatial and seasonal differences should be considered in decadal climate predictions.

In comparison with the spatial distribution (Fig. 8a–d, left panels) of high-value areas for monthly SST decadal PLs (Fig. 2), these seasonal distributions reveal distinct differences. The North Pacific Ocean basin typically shows high decadal PLs, although there are notable seasonal variations. For example, the high-value area (over 10 years) in the eastern North Pacific Ocean (0° – 50°N, 140° – 110°W) diminishes in summer compared to spring, while in autumn, the decadal PL in the northwest Pacific Ocean (10° – 45°N, 110° – 135°E) decreases to a range of about 8 years. Conversely, the South Pacific Ocean exhibits a patchy distribution of high-predictability regions, primarily in the central (10° – 40°S, 180° – 125°W) and eastern (10° – 30°S, 120° – 70°W) areas. While these regions exhibit relatively high PLs in boreal spring and autumn, the central high-value area diminishes in summer and is largely restricted to the Southern Ocean in winter. Overall, the decadal PLs in the Pacific Ocean basin exhibit asymmetry between the NH and SH, with larger PLs and more extensive high-value areas in NH.

The decadal PL in the Indian Ocean basin exhibits significant seasonal differences. During boreal summer, the overall decadal PL reaches its highest value, significantly exceeding that of other seasons. In contrast, high PLs (over 10 years) in other seasons are restricted to localized regions. For instance, in winter, the high-value areas are restricted to a limited section of the southern Indian Ocean (5° – 20°S, 70° – 90°E), while other regions exhibit PLs below 8 years. In spring, high PLs are primarily observed in the tropical eastern Indian Ocean and the Maritime Continent (5°N – 20°S, 80° – 115°E), while the decadal PLs to the west of this area are lower (about 4–7 years). In autumn, high-value regions are mainly found in the Arabian Sea (0° – 20°N, 45° – 80°E), the Bay of Bengal (0° – 25°N, 80° – 100°E), and multiple patchy areas in the southern Indian Ocean. Overall, decadal predictability of SST in the Indian Ocean is more difficult in seasons other than summer, with winter being the most challenging.

In the Atlantic Ocean basin, decadal PLs are elevated during summer and autumn, with autumn displaying the

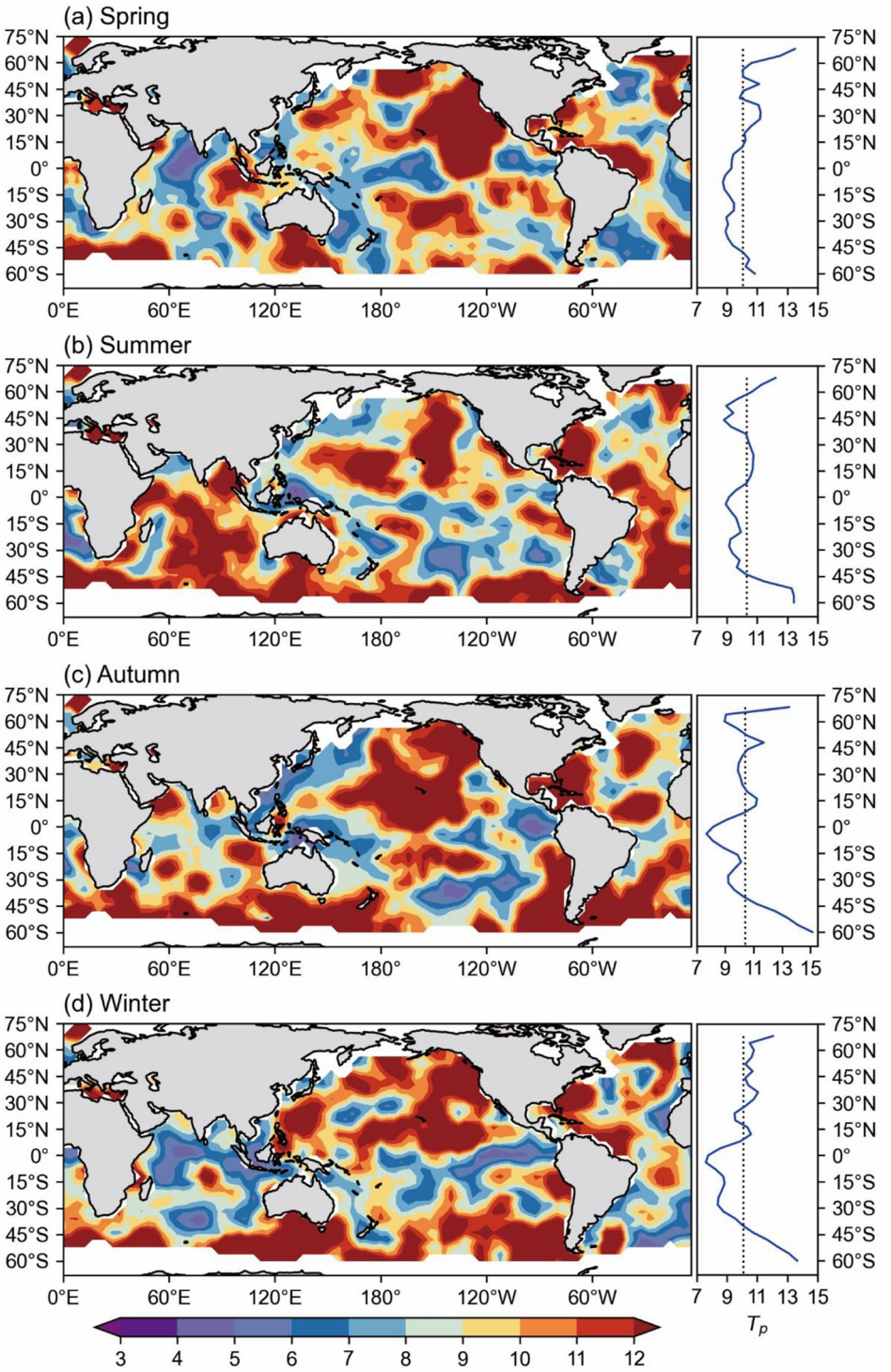

Fig. 8 Spatial distribution (left) of the seasonal mean SST predictability limit (T_p, in years) estimated by the OLDA algorithm for the 9-year low-pass filtered ERSST V5 dataset, and their zonal mean profile (blue solid line) on the right, with the global mean (black dashed line). **a** Spring (March – May), **b** summer (June – August), **c** autumn (September – November), **d** winter (December – February)

highest values, followed by summer. Conversely, winter and spring generally show lower PLs. During winter and spring, high predictability is mainly observed in the NH, while the South Atlantic Ocean basin shows relatively lower values. Specifically, high decadal PLs (over 9 years) are consistently observed across all seasons in the Gulf Stream region (15° – 45°N, 95° – 60°W), the western tropical North Atlantic Ocean (0° – 20°N, 55° – 20°W), and the mid to high latitude areas of the North Atlantic Ocean (30° – 65°N, 35° – 5°W). In comparison, the mid-latitude region of the North Atlantic Ocean (35° – 60°N, 55° – 25°W) exhibits lower PLs (blow 8 years) during spring and summer.

The Southern Ocean (30° – 65°S, 0° – 360°E) also exhibits significant seasonal differences in decadal PLs. Overall,

decadal PLs remain relatively high across all seasons, which contrasts with the lower predictability observed on the interannual scale (Li and Ding 2013). However, the distribution of high-value areas varies significantly across seasons. Spring displays a lower decadal PL compared to other seasons. This reduction is mainly attributed to the lower zonal mean predictability in the mid to high latitudes (50° – 65°S) during spring. The presence of these low-value areas in spring primarily drives the overall reduction in predictability for that season.

In summary, the decadal PLs of SST reveal significant seasonal differences across various ocean basins. A comprehensive analysis of these seasonal patterns is essential for understanding long-term SST trends and to enhance decadal SST predictions. Estimations of the decadal PLs of different seasonal mean SSTs provide clearer insights into ocean–atmosphere interactions and enhance our capacity for precise decadal climate predictions.

5.2 Seasonal differences in decadal PLs of SLP

The decadal PLs of SLP show significant seasonal differences (Fig. 9), which differ notably from the seasonal patterns observed in SST (Fig. 8). In general, the global mean PL in the NH is relatively high in spring (about 10 years), whereas in other seasons, it is slightly lower (about 9 years). However, the latitudinal distribution of high PL regions varies considerably between seasons. In spring, the mid and low latitudes regions (45°N – 45°S) in both hemispheres demonstrate relatively high PLs, which range from 10 to 12 years (Fig. 9a, right panel). In contrast, the tropical SST PL is lower in spring (Fig. 8a, right panel), which suggests that the predictability of tropical SLP may be influenced by both tropical and extratropical SST. The other seasons exhibit similar patterns. Summer displays high PLs regions in the NH mid-to-low latitudes (0° – 60°N) and the SH mid-to-high latitudes (50° – 75°S), where PLs are over 9 years (Fig. 9b, right panel). Autumn shows comparable PLs between hemispheres but with particularly high values in the tropical (25°N – 25°S) and SH high-latitude (60° – 85°S) regions (Fig. 9c, right panel). And winter concentrates PL primarily in the SH mid-to-high latitudes(45° – 85°S) (Fig. 9d, right panel).

A comparison of these patterns with the zonal profiles of SST (Fig. 8) reveals that high decadal PLs of SST do not necessarily coincide with high PLs of SLP in the same region. This complexity in ocean–atmosphere interactions emphasizes the necessity of a thorough investigation into these relationships to enhance our comprehension of decadal predictability.

Figure 9a–d (left panels) illustrate the spatial distribution of seasonal mean decadal PLs of SLP for boreal spring (MAM), summer (JJA), autumn (SON), and winter (DJF), which highlight notable seasonal differences in these PLs. Compared to the monthly results (Fig. 5, left panels), new patterns emerge. In the NH high-latitude regions (65° – 85°N, 0° – 360°E), decadal PLs are generally lower, with high-PL regions being localized. For instance, in summer, the East Siberian Sea–Beaufort Sea region (65° – 85°N, 150°E – 130°W) exhibits relatively high decadal PL (over 10 years, Fig. 9b). In the SH mid-to-high latitudes (30° – 85°S, 0° – 360°E), high PLs are observed across seasons, including regions south of Africa (50° – 85°S, 0° – 80°E), the South Pacific Ocean (40° – 80°S, 160°E – 80°W), and the South Atlantic Ocean (30° – 70°S, 60° – 0°W). However, these regions experience lower PLs in summer (Fig. 9b), with similar reductions observed in the South Pacific Ocean during autumn. In mid-to-low latitudes, the Indian Ocean–Eurasia–Africa region (55°N – 15°S, 0° – 105°E) consistently shows high PLs, particularly in spring and summer. The mid-to-low latitudes of the Pacific Ocean display high decadal PLs in spring, with this limit concentrated in the Maritime Continent–Northwest Pacific Ocean (50°N – 10°S, 110°E – 170°W) during summer (Fig. 9b). In autumn and winter, decadal PLs generally decrease, with high-value areas that appear in patches; during winter, especially high limits are found in the East Asia – Maritime Continent – Australia region west of the Pacific Ocean (Fig. 9c, d). In the Americas–Atlantic Ocean mid-to-low latitudes, high-value regions shift in a strip-like pattern across seasons, with a focus on the North American West Coast–North Atlantic Ocean mid-latitudes (10° – 55°N, 120° – 5°W) during summer and in the South American–Atlantic Ocean mid-to-low latitudes (15°N – 45°S, 80° – 0°W) during other seasons. Moreover, our results reveal relatively high decadal PLs of SLP in monsoon regions, even though predicting interannual variability in these areas remains challenging. For example, in South Asia and East Asia, SLP decadal PLs exhibit seasonal differences, potentially driven by decadal-scale SST variability, solar activity, and seasonal variations of other factors (Watanabe and Yamazaki 2014; Dong et al. 2016a; Jin et al. 2019). However, the mechanisms influencing the decadal PLs of SLP, particularly their seasonal differences, require further investigation. Our seasonal analyses suggest that decadal PLs could guide further studies to improve predictive capabilities for monsoon regions.

The decadal PLs of SLP do not completely correspond to those of SST (Fig. 8), which suggests that decadal

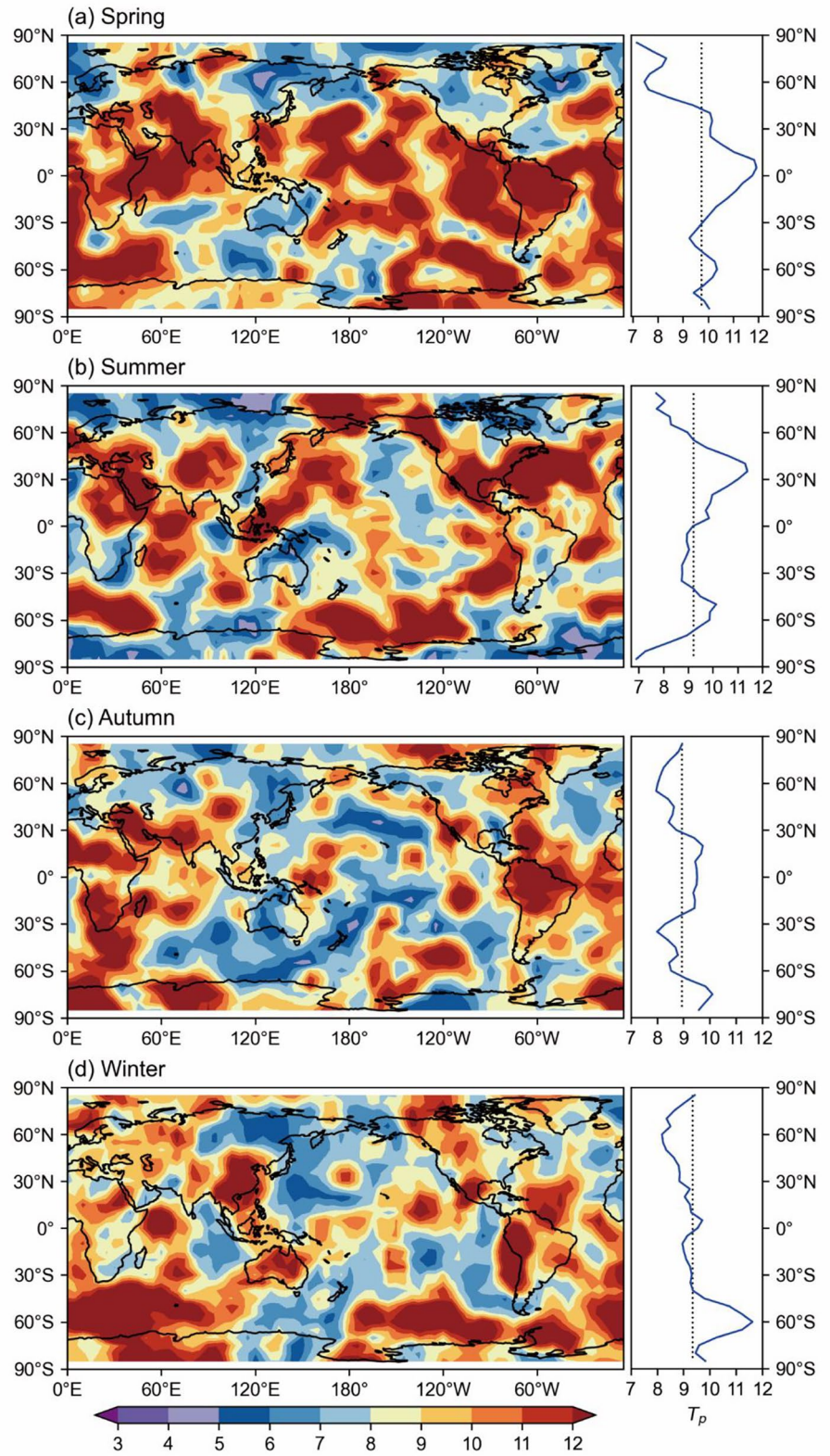

Fig. 9 As in Fig. 8, but for the seasonal mean SLP predictability limit (T_p, in years) based on the 9-year low-pass filtered monthly HadSLP2r dataset

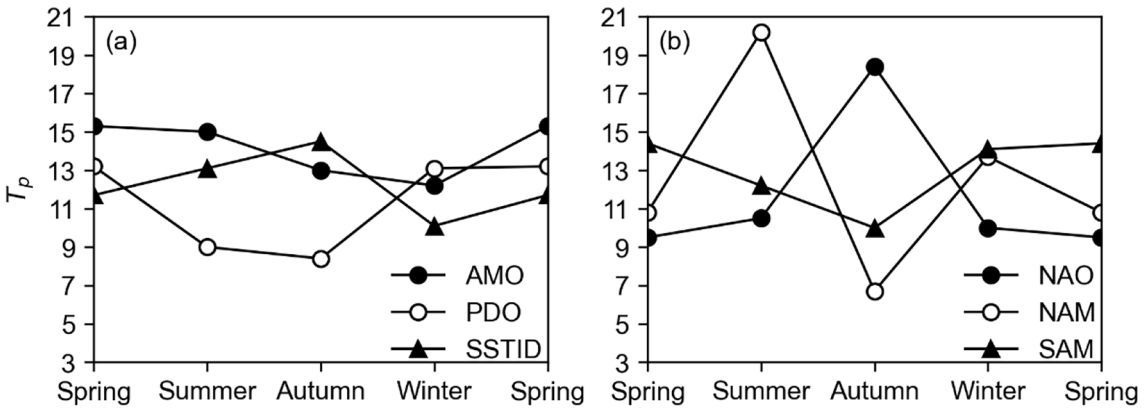

Fig. 10 **a** Seasonal variations in the decadal predictability limit (T_p, in years) of monthly seasonal averaged of the AMO (closed circle) index, PDO (open circle) index and SSTID (closed triangle) index, obtained using OLDA algorithm. **b** As in **a**, but for the NAO (closed circle) index, NAM (open circle) index, and SAM (closed triangle) index

atmospheric predictability is influenced not only by local SST but also by remote SSTs and land–atmosphere interactions. This highlights the complexity of decadal processes in the ocean–atmosphere system and the challenges in decadal prediction.

5.3 Seasonal differences in decadal pls of major decadal modes

Based on the OLDA algorithm, Fig. 10a illustrates the decadal PLs of the major decadal modes of SST for each season and reveals distinct seasonal characteristics. The AMO index exhibits relatively high decadal PLs (about 15 years) in spring and summer in the NH, compared to approximately 13 years in autumn and 12 years in winter, indicating stronger predictability during spring and summer relative to autumn and winter. For the PDO index, decadal PLs are higher in spring and winter (about 13 years) but decrease to approximately 9 years in summer and about 8 years in autumn, which shows stronger predictability in winter and spring and weaker predictability in summer and autumn. Although previous studies have observed that the PDO index reaches higher values around May and June (Wang et al. 2012), this study reveals seasonal variations in its decadal PLs that merit further investigation. In contrast, the SSTID index shows a notable difference from the AMO and PDO indices, with its highest decadal PL of about 15 years in autumn, and the lowest limit of about 10 years in winter, while spring and summer show intermediate values of about 12 and 13 years, respectively.

The decadal PLs of the AMO exhibit less pronounced seasonal differences compared to the PDO and SSTID, which indicates greater stability. These seasonal differences provide valuable insights into the variation of SST modes on the decadal scale across different seasons and are significant for long-term climate prediction.

Figure 10b illustrates the decadal PLs of the major decadal modes of SLP for each season, as derived from the OLDA algorithm. The NAO index has the highest decadal PL in autumn (about 18 years), while the limits in other seasons are similar, around 10 years. The decadal PL of the NAM index is most significant in summer in the NH (about 20 years). In contrast, the PL in autumn is the lowest, at only about 7 years; in spring and winter, it is about 11 years and 14 years, respectively. Although these values are lower than in summer, they still indicate substantial decadal predictability. Notably, the meridional scale of NAM in summer is relatively small, with its action centers located in the Arctic Ocean (summer) and Greenland (winter) (Ogi et al. 2004). The decadal PL of the SAM index is about 14 years in both spring and winter, higher than in other seasons. The PL in autumn is the lowest at about 10 years, while in summer, it is about 12 years, which also reflects significant predictability.

In summary, the NAM index exhibits greater seasonal differences (with a range of about 13 years) compared to other modes, and the seasonal differences in the NAO and NAM indices are more pronounced than those observed in the decadal SST modes. This suggests that, compared to major ocean decadal modes, the primary SLP modes exhibit greater seasonal instability on the decadal scale, which potentially makes them more challenging to predict. We also used the $\mathrm{OLDA_E}$ algorithm to perform a quantitative estimation of seasonal means for SST, SLP, and major decadal modes. The results are generally consistent with those

obtained with the OLDA algorithm and are therefore not discussed in detail here (see Figs. S1–S3 in Supplementary).

6 Conclusions and discussion

This study focuses on the decadal PLs of key oceanic and atmospheric variables using the NLLE method and offers a comprehensive evaluation of spatial and temporal variability in decadal PLs, through the application of the OLDA algorithm that enhances traditional LDA algorithms by optimizing the EW τ. The effectiveness of the OLDA algorithm was demonstrated through its application to the Lorenz63 system, where it showed significant improvements in the RGIE compared to the LDA algorithm. This illustrates that OLDA more accurately captures the PL in nonlinear systems and can effectively be applied to real-world datasets.

We examined the spatial distribution of the decadal PL of the 9-year low-pass filtered SST and SLP fields, revealing significant regional differences. For SST, the PL ranges from about 8 to 17 years, with considerable variability across ocean basins, and exhibits an asymmetry between the NH and SH. The Southern Ocean shows generally higher predictability and a zonal banded pattern around the hemisphere, with values exceeding 10 years. In the eastern North Pacific Ocean, a large region of high predictability is observed, while the North Atlantic Ocean also exhibits an elevated PL. Key areas with high predictability (over 10 years) include the Gulf Stream region, the mid-latitude North Atlantic Ocean, and the tropical North Atlantic Ocean. Additionally, certain regions of the Arabian Sea and the Maritime Continent exhibit a relatively high PL (about $8-12$ years). In contrast, the tropical central-eastern Pacific Ocean and the western North Pacific Ocean show lower PLs, with values below 7 years. For SLP, the decadal PL ranges from about 8 to 11 years, slightly lower than that of SST. In general, the SH shows higher predictability than the NH. The high-value regions for SLP are more dispersed, primarily located in the mid to high latitudes south of Africa, the NH high latitudes, and other areas such as the northwest Pacific Ocean, central-eastern Pacific Ocean, southern Indian Ocean, central Africa, the Arabian Peninsula to East Asia, and South America. In these areas, the PLs exceeds 10 years. However, the areas of high SLP decadal PLs do not completely correspond with those of SST in terms of spatial distribution. While some regions, such as the central-eastern Pacific Ocean and subtropical North Atlantic Ocean, exhibit high predictability of both SLP and SST, other regions, like the northwest Pacific Ocean and southern Indian Ocean, show a significant disparity between the two variables. This indicates that local SST variability does not entirely dictate SLP predictability, suggesting that other factors or teleconnections might contribute to the higher predictability of SLP in these regions. Based on the spatial distribution analysis of SST and SLP decadal PLs, we performed a regional average of the time series in key regions. For SST, these regions include the eastern North Pacific Ocean, the Gulf Stream, the mid-latitude North Atlantic Ocean, the tropical North Atlantic Ocean, the Arabian Sea, the Maritime Continent, the eastern South Pacific Ocean, and the Southern Ocean. For SLP, the key regions span the mid to high latitudes south of Africa, the southeastern Pacific Ocean, the southwestern Atlantic Ocean, NH high latitudes, the Arabian Peninsula-northwestern Pacific Ocean, the eastern North Pacific Ocean-central America, the subtropical North Atlantic Ocean, the southern Indian Ocean, the central Africa, the northern North America, and the south America. The results indicate that the decadal PLs in these areas exceed 10 years, highlighting significant long-term predictability.

For a more comprehensive understanding of the decadal predictability characteristics, we also analyzed seasonal differences. Both SST and SLP decadal PLs exhibit significant seasonal differences. SST PLs are slightly higher during boreal summer and autumn compared to spring and winter, with obvious differences across different ocean basins. In the Pacific Ocean, the NH generally shows higher PLs; however, there are significant seasonal changes, such as the reduction of high value areas in the eastern North Pacific during summer and a decrease to 5–8 years in the northwest Pacific during autumn. The Indian Ocean has its highest PLs during boreal summer, while winter poses challenges for predictability, with some localized regions showing PLs below 8 years. In the Atlantic Ocean, elevated PLs (over 9 years) are found in summer and autumn, particularly in the Gulf Stream region, while lower values are observed in spring and winter. The Southern Ocean maintains relatively high PLs across all seasons, although there is a notable reduction in spring. In contrast, the seasonal differences in SLP decadal PLs differ from those of SST, with a global mean PL of about 10 years in boreal spring, compared to about 9 years in the other seasons. Spring shows relatively high PLs (over 10 years) in mid and low latitudes regions of both hemispheres, while summer features high PLs in the NH mid to low latitudes and the SH mid to high latitudes (over 9 years). Autumn displays similar patterns across both hemispheres, with high values in the tropical and SH high-latitude regions, and winter concentrates high PLs primarily in the SH mid to high latitudes. Notably, high PLs of SST and SLP in the same region do not necessarily coincide, underscoring the complexity of ocean–atmosphere interactions.

This study further estimates the decadal PLs of major SST and SLP climate modes and reveals distinct patterns. Among SST modes, the SSTID stands out with the longest PL of about 17 years, which functions as a global-scale decadal mode. It is followed by the AMO (about 14 years) and the PDO (about 13 years). The interaction between SSTID

and the regional expressions of AMO and PDO emphasizes their unique roles. In the case of SLP modes, the NAO shows the longest PL of about 16 years, while the SAM (about 15 years) and NAM (about 11 years) have shorter PLs. Seasonal variations are significant for both SST and SLP modes. The AMO index demonstrates relatively high decadal PLs (about 15 years) during boreal spring and summer, which decrease in autumn (about 13 years) and winter (about 12 years). In contrast, the PDO index shows higher PLs in spring and winter (about 13 years), lower in summer and autumn. The SSTID index reaches its highest value in autumn (about 15 years) and drops to about 10 years in winter, with spring and summer PLs around 12 and 13 years, respectively. This indicates that the AMO index remains relatively stable with minimal seasonal differences. Meanwhile, significant seasonal variability is evident in SLP modes. The NAO index has the highest PL in autumn (about 18 years), while other seasons around 10 years. The NAM index reaches its maximum in the boreal summer (about 20 years), but declines to its lowest in autumn at about 7 years, with spring and winter values about 11 and 14 years, respectively. The SAM index maintains PLs of about 14 years in spring and winter, higher than in other seasons, while autumn records the lowest at around 10 years and summer at about 12 years. Overall, major SLP modes like the NAM show greater seasonal variability than other modes, which indicates that their decadal predictability varies significantly with the seasons and increases their complexity.

Comparison with previous studies (Ding et al. 2016) demonstrates that the OLDA algorithm provides higher and more precise estimates of decadal PLs. While Ding et al. (2016) reported quantitatively estimated PLs of SST ranged from 4 to 12 years and PLs of SLP were 4–7 years, our results consistently indicate higher PLs for both variables. Additionally, the PLs of major decadal climate modes, such as the PDO and NAO, are notably higher in our study. Our analysis identifies more extensive high-PL regions and seasonal differences in PL quantitative estimates, which together demonstrate the broader applicability and effectiveness of the OLDA algorithm in capturing decadal predictability. Although the SST and SLP datasets used in this study differ in spatial resolution, decadal variability occurs on long temporal scales, which typically correspond to large spatial scales. This correspondence reduces the sensitivity of the results to differences in resolution and allows for an adequate representation of large-scale patterns. To further validate these results, we conducted additional estimations using the HadISST dataset (Rayner et al. 2003), covering the period from January 1870 to December 2023 (see Figure S4 in Supplementary).

The decadal PLs estimated in this study of SST, SLP, and their seasonal differences provide a useful reference for evaluating decadal prediction skill. Current decadal prediction efforts for SST show relatively high skill in regions such as the North Atlantic Ocean, Indian Ocean, and North Pacific, with ensemble models achieving reasonable skill within a about 2–5 years range (Boer and Sospedra-Alfonso 2019; Ruprich-Robert et al. 2021; Pan et al. 2022; Zhou et al. 2024). However, these models tend to underestimate decadal variability compared to the PLs estimated in our study, which extend up to about 17 years, indicating a substantial gap between current prediction skill and potential predictability. For SLP, the predictive skill is generally lower than that of SST, though it has improved with better initialization and multi-model approaches (Boer et al. 2016; Smith et al. 2019; Nicolì et al. 2023). However, our study estimates the PLs of SLP to range from about 8 to 11 years, which are comparable to or even exceed those of SST in certain regions. This suggests the need for further improvement in SLP decadal prediction methods. Although much of the existing research has focused on decadal variability in the North Atlantic Ocean and North Pacific Ocean, our findings reveal that other regions also exhibit high PLs. This suggests the need to expand the scope of future research to include these regions, rather than focusing solely on the traditionally studied areas. Additionally, while some studies have addressed seasonal differences in predictability (Müller et al. 2012; Yeager et al. 2018; Düsterhus and Brune 2024), our analysis shows considerable room for improvement across various seasons.

Future research should further investigate the factors driving decadal SST variability and its broader effects, and examine why the decadal PL of SLP does not completely match regions of high SST. Atmospheric decadal predictability is influenced by multiple factors, including changes in SST, sea ice, stratospheric conditions, the QBO, and seasonal variations. Further investigation into these factors will improve our understanding of the decadal processes within the ocean–atmosphere system and enhance the accuracy of long-term climate predictions, particularly in under-researched regions like the SH.

Appendix A: detailed parameters of the OLDA and OLDAE algorithms

Table 2 presents the detailed parameters used for the OLDA algorithm in this study, while Table 3 provides the detailed parameters for the $OLDA_E$ algorithm used in this study.

Table 2 Detailed parameters of the OLDA algorithm

Initial state set ($\boldsymbol{A}_i$)	Local EW (τ_L)	Number of analog states (m_i)			
$\boldsymbol{A}_0$	0	$m_0 > 400$	$m_0 \in [200, 399]$	$m_0 \in [40,200]$	$m_0 \leq 39$
$\boldsymbol{A}_1$	$0.1 \times T_{p0}$	$m_1 = 0.1 \times m_0$	$m_1 = 0.2 \times m_0$	$m_1 = 40$	$m_1 = \frac{m_0}{2} + 1$
$\boldsymbol{A}_2$	$0.2 \times T_{p0}$	$m_2 = 20$			$m_2 = \frac{m_1}{2} + 1$
$\boldsymbol{A}_3$	$0.3 \times T_{p0}$	$m_3 = 10$			$m_3 = \frac{m_2}{2} + 1$
$\boldsymbol{A}_4$	$0.4 \times T_{p0}$	$m_4 = 5$			$m_4 = \frac{m_3}{2} + 1$
$\boldsymbol{A}_5$	$0.5 \times T_{p0}$	$m_5 = 1$			

Table 3 Detailed parameters of the OLDA_E algorithm

Initial state set ($\boldsymbol{A}_i$)	Local EW (τ_L)	Number of analog states (m_i)			
$\boldsymbol{A}_0$	0	$m_0 > 200$	$m_0 \in [60, 200]$	$m_0 \in [10, 59]$	$m_0 < 10$
$\boldsymbol{A}_1$	$0.1 \times T_{p0}$	$m_1 = 0.3 \times m_0$	$m_1 = 60$	$m_1 = 9$	$m_1 = \frac{m_0}{2} + 1$
$\boldsymbol{A}_2$	$0.2 \times T_{p0}$	$m_2 = 40$		$m_2 = 8$	$m_2 = \frac{m_1}{2} + 1$
$\boldsymbol{A}_3$	$0.3 \times T_{p0}$	$m_3 = 20$		$m_3 = 7$	$m_3 = \frac{m_2}{2} + 1$
$\boldsymbol{A}_4$	$0.4 \times T_{p0}$	$m_4 = 10$		$m_4 = 6$	$m_4 = \frac{m_3}{2} + 1$
$\boldsymbol{A}_5$	$0.5 \times T_{p0}$	$m_5 = 5$			$m_5 = 1$

Supplementary Information The online version contains supplementary material available at https://doi.org/10.1007/s00382-024-07573-9.

Acknowledgements This work was jointly sponsored by National Natural Science Foundation of China (NSFC) Project (42130607), National Key R&D Program of China (2023YFF0805100), and Laoshan Laboratory (No. LSKJ202202600). We are grateful to the NOAA and UK Met Office Hadley Centre for providing the reanalysis data, the NOAA for providing the global warming trend time series, and the NOAA-PSL for providing the AMO and SAM index time series. We thank Ms. Qirong An, Ms. Ran An, Ms. Xinxin Tang and Ms. Yue Sun for their help during the preparation of the manuscript.

Author contributions JL conceived the idea. All authors contributed to the study conception and design. Material preparation, data collection and analysis were performed by RL, RS, SZ, and HS. The first draft of the manuscript was written by RL and ZH and all authors commented on previous versions of the manuscript. All authors read and approved the final manuscript.

Funding This work is supported by National Natural Science Foundation of China (NSFC) Project (42130607), National Key R&D Program of China (2023YFF0805100), and Laoshan Laboratory (No. LSKJ202202600).

Data availability The data that support the findings of this study are freely available. The ERSST.v5 data can be obtained from https://climatedataguide.ucar.edu/climate-data/sst-data-noaa-extended-reconstruction-ssts-version-5-ersstv5. The HadSLP2r dataset is available at https://www.metoffice.gov.uk/hadobs/hadslp2/. The AMO index can be obtained from https://psl.noaa.gov/data/gridded/data.kaplan_sst.html. The NAM and NAO index can be obtained from http://lijianping.cn/dct/page/65540. The SAM index is available at https://psl.noaa.gov/data/20thC_Rean/timeseries/monthly/SAM/sam.20crv3.long.data. The global warming trend time series can be obtained from https://www.ncdc.noaa.gov/cag/global/time-series.

Declarations

Conflict of interest The authors have no relevant financial or non-financial interests to disclose.

References

Allan R, Ansell T (2006) A new globally complete monthly historical gridded mean sea level pressure dataset (HadSLP2): 1850–2004. J Clim 19:5816–5842. https://doi.org/10.1175/JCLI3937.1

An QR, Li JP, Yang JJ (2024) Evaluation of sea surface temperature interhemispheric dipole in CMIP6 historical simulations. Clim Dyn. https://doi.org/10.1007/s00382-024-07455-0

Athanasiadis PJ, Yeager S, Kwon Y-O et al (2020) Decadal predictability of North Atlantic blocking and the NAO. Npj Clim Atmos Sci 3:20. https://doi.org/10.1038/s41612-020-0120-6

Boer GJ (2000) A study of atmosphere-ocean predictability on long time scales. Clim Dyn 16:469–477. https://doi.org/10.1007/s003820050340

Boer GJ (2004) Long time-scale potential predictability in an ensemble of coupled climate models. Clim Dyn 23:29–44. https://doi.org/10.1007/s00382-004-0419-8

Boer GJ (2011) Decadal potential predictability of twenty-first century climate. Clim Dyn 36:1119–1133. https://doi.org/10.1007/s00382-010-0747-9

Boer GJ, Lambert SJ (2008) Multi-model decadal potential predictability of precipitation and temperature. Geophys Res Lett 35:L05706. https://doi.org/10.1029/2008GL033234

Boer GJ, Sospedra-Alfonso R (2019) Assessing the skill of the Pacific Decadal Oscillation (PDO) in a decadal prediction experiment. Clim Dyn 53:5763–5775. https://doi.org/10.1007/s00382-019-04896-w

Boer GJ, Smith DM, Cassou C et al (2016) The decadal climate prediction project (DCPP) contribution to CMIP6. Geosci Model Dev 9:3751–3777. https://doi.org/10.5194/gmd-9-3751-2016

Bond NA, Overland JE, Spillane M, Stabeno P (2003) Recent shifts in the state of the North Pacific. Geophys Res Lett 30:2183. https://doi.org/10.1029/2003GL018597

Carton JA, Cao X, Giese BS, Silva AMD (1996) Decadal and interannual sst variability in the tropical Atlantic ocean. J Phys Ocean 26:1165–1175

Chen BH, Li JP, Ding RQ (2006) Nonlinear local Lyapunov exponent and atmospheric predictability research. Sci China D Earth Sci 49:1111–1120. https://doi.org/10.1007/s11430-006-1111-0

Chikamoto Y, Mochizuki T, Timmermann A et al (2016) Potential tropical Atlantic impacts on Pacific decadal climate trends. Geophys Res Lett 43:7143–7151. https://doi.org/10.1002/2016GL069544

Choi J, Son S-W (2022) Seasonal-to-decadal prediction of El Niño-southern oscillation and pacific decadal oscillation. Npj Clim Atmos Sci 5:29. https://doi.org/10.1038/s41612-022-00251-9

Collins M (2002) Climate predictability on interannual to decadal time scales: the initial value problem. Clim Dyn 19:671–692. https://doi.org/10.1007/s00382-002-0254-8

Collins M, Sinha B (2003) Predictability of decadal variations in the thermohaline circulation and climate. Geophys Res Lett 30:1306. https://doi.org/10.1029/2002GL016504

Deser C, Phillips AS (2021) Defining the internal component of atlantic multidecadal variability in a changing climate. Geophys Res Lett 48:e2021GL095023. https://doi.org/10.1029/2021GL095023

Di Lorenzo E, Schneider N, Cobb KM et al (2008) North Pacific Gyre Oscillation links ocean climate and ecosystem change. Geophys Res Lett 35:2007GL032838. https://doi.org/10.1029/2007GL032838

Ding RQ, Li JP (2007) Nonlinear finite-time Lyapunov exponent and predictability. Phys Lett A 364:396–400. https://doi.org/10.1016/j.physleta.2006.11.094

Ding RQ, Li JP (2011) Comparisons of two ensemble mean methods in measuring the average error growth and the predictability. Acta Meteorol Sin 25:395–404. https://doi.org/10.1007/s13351-011-0401-4

Ding RQ, Li JP, Seo K-H (2010) Predictability of the Madden–Julian oscillation estimated using observational data. Mon Weather Rev 138:1004–1013. https://doi.org/10.1175/2009MWR3082.1

Ding RQ, Li JP, Seo K-H (2011) Estimate of the predictability of boreal summer and winter intraseasonal oscillations from observations. Mon Weather Rev 139:2421–2438. https://doi.org/10.1175/2011MWR3571.1

Ding RQ, Li JP, Zheng F et al (2016) Estimating the limit of decadal-scale climate predictability using observational data. Clim Dyn 46:1563–1580. https://doi.org/10.1007/s00382-015-2662-6

Doblas-Reyes FJ, Andreu-Burillo I, Chikamoto Y et al (2013) Initialized near-term regional climate change prediction. Nat Commun 4:1715. https://doi.org/10.1038/ncomms2704

Dong L, McPhaden MJ (2017) Why has the relationship between Indian and Pacific ocean decadal variability changed in recent decades? J Clim 30:1971–1983. https://doi.org/10.1175/JCLI-D-16-0313.1

Dong BW, Sutton RT, Highwood EJ, Wilcox LJ (2016a) Preferred response of the East Asian summer monsoon to local and non-local anthropogenic sulphur dioxide emissions. Clim Dyn 46:1733–1751. https://doi.org/10.1007/s00382-015-2671-5

Dong L, Zhou TJ, Dai AG et al (2016b) The footprint of the inter-decadal pacific oscillation in Indian ocean sea surface temperatures. Sci Rep 6:21251. https://doi.org/10.1038/srep21251

Düsterhus A, Brune S (2024) Decadal predictability of seasonal temperature distributions. Geophys Res Lett 51:e2023GL107838. https://doi.org/10.1029/2023GL107838

Enfield DB, Mestas-Nuñez AM, Trimble PJ (2001) The Atlantic multidecadal oscillation and its relation to rainfall and river flows in the continental U.S. Geophys Res Lett 28:2077–2080. https://doi.org/10.1029/2000GL012745

Feng J, Li JP, Li Y (2010) Is there a relationship between the SAM and southwest Western Australian winter rainfall? J Clim 23:6082–6089. https://doi.org/10.1175/2010JCLI3667.1

Feng JQ, Hu DX, Yu LJ (2012) Low-frequency coupled atmosphere-ocean variability in the southern Indian Ocean. Adv Atmos Sci 29:544–560. https://doi.org/10.1007/s00376-011-1096-2

Feng P-N, Lin H, Derome J, Merlis TM (2021) Forecast skill of the NAO in the subseasonal to-seasonal prediction models. J Clim. https://doi.org/10.1175/JCLI-D-20-0430.1

Gong DY, Wang SW (1999) Definition of Antarctic oscillation index. Geophys Res Lett 26:459–462. https://doi.org/10.1029/1999GL900003

Griffies SM, Bryan K (1997) A predictability study of simulated North Atlantic multidecadal variability. Clim Dyn 13:459–487. https://doi.org/10.1007/s003820050177

Han WQ, Vialard J, McPhaden MJ et al (2014) Indian ocean decadal variability: a review. Bull Am Meteorol Soc 95:1679–1703. https://doi.org/10.1175/BAMS-D-13-00028.1

Ho CK, Hawkins E, Shaffrey L, Underwood FM (2013) Statistical decadal predictions for sea surface temperatures: a benchmark for dynamical GCM predictions. Clim Dyn 41:917–935. https://doi.org/10.1007/s00382-012-1531-9

Hou ZL, Li JP, Ding RQ, Feng J (2022) Investigating decadal variations of the seasonal predictability limit of sea surface temperature in the tropical Pacific. Clim Dyn 59:1079–1096. https://doi.org/10.1007/s00382-022-06179-3

Hou ZL, Li JP, Diao YN et al (2024) Asymmetric influences of ENSO phases on the predictability of north pacific sea surface temperature. Geophys Res Lett 51:e2023GL108091. https://doi.org/10.1029/2023GL108091

Hu YY, Tung KK (2002) Interannual and decadal variations of planetary wave activity, stratospheric cooling, and northern hemisphere annular mode. J Clim 15:1659–1673. https://doi.org/10.1175/1520-0442(2002)015%3c1659:IADVOP%3e2.0.CO;2

Huai XW, Li JP, Ding RQ, Liu DQ (2017) Optimal evolutionary window for the nonlinear local lyapunov exponent. SOLA 13:125–129. https://doi.org/10.2151/sola.2017-023

Huang BY, Thorne PW, Banzon VF et al (2017) Extended reconstructed sea surface temperature, version 5 (ERSSTv5): upgrades, validations, and intercomparisons. J Clim 30:8179–8205. https://doi.org/10.1175/JCLI-D-16-0836.1

Huang BY, Menne MJ, Boyer T et al (2020) Uncertainty estimates for sea surface temperature and land surface air temperature in NOAAGlobalTemp version 5. J Clim 33:1351–1379. https://doi.org/10.1175/JCLI-D-19-0395.1

Huang BY, Yin X, Menne MJ et al (2022) Improvements to the land surface air temperature reconstruction in NOAAGlobalTemp: an artificial neural network approach. Artif Intell Earth Syst 1:e220032. https://doi.org/10.1175/AIES-D-22-0032.1

Jin C, Liu J, Wang B et al (2019) Decadal variations of the east asian summer monsoon forced by the 11-year insolation cycle. J Clim 32:2735–2745. https://doi.org/10.1175/JCLI-D-18-0288.1

Joh Y, Delworth TL, Wittenberg AT et al (2022) Stronger decadal variability of the Kuroshio Extension under simulated future climate change. Npj Clim Atmos Sci 5:1–9. https://doi.org/10.1038/s41612-022-00285-z

Kerr RA (2000) A north Atlantic climate pacemaker for the centuries. Science 288:1984–1985. https://doi.org/10.1126/science.288.5473.1984

Kim H-M, Webster PJ, Curry JA (2012) Evaluation of short-term climate change prediction in multi-model CMIP5 decadal hindcasts.

Geophys Res Lett 39:L10701. https://doi.org/10.1029/2012GL051644
King J, Anchukaitis KJ, Allen K et al (2023) Trends and variability in the southern annular mode over the common era. Nat Commun 14:2324. https://doi.org/10.1038/s41467-023-37643-1
Krishnamurthy L, Krishnamurthy V (2016) Decadal and interannual variability of the Indian ocean SST. Clim Dyn 46:57–70. https://doi.org/10.1007/s00382-015-2568-3
Kushnir Y, Scaife AA, Arritt R et al (2019) Towards operational predictions of the near-term climate. Nat Clim Change 9:94–101. https://doi.org/10.1038/s41558-018-0359-7
Latif M, Collins M, Pohlmann H, Keenlyside N (2006) A review of predictability studies of atlantic sector climate on decadal time scales. J Clim 19:5971–5987. https://doi.org/10.1175/JCLI3945.1
Lee J-Y, Marotzke J, Bala G et al (2021) Future global climate: scenario-based projections and near-term information. In: Masson-Delmotte V, Zhai P, Pirani A et al (eds) Climate change 2021: the physical science basis. Contribution of working group I to the sixth assessment report of the intergovernmental panel on climate change. Cambridge University Press, Cambridge, pp 553–672
Levine AFZ, McPhaden MJ, Frierson DMW (2017) The impact of the AMO on multidecadal ENSO variability. Geophys Res Lett 44:3877–3886. https://doi.org/10.1002/2017GL072524
Li JP, Ding RQ (2011) Temporal-spatial distribution of atmospheric predictability limit by local dynamical analogs. Mon Weather Rev 139:3265–3283. https://doi.org/10.1175/MWR-D-10-05020.1
Li JP, Ding RQ (2013) Temporal–spatial distribution of the predictability limit of monthly sea surface temperature in the global oceans. Int J Climatol 33:1936–1947. https://doi.org/10.1002/joc.3562
Li JP, Wang JXL (2003a) A modified zonal index and its physical sense. Geophys Res Lett 30:1632. https://doi.org/10.1029/2003GL017441
Li JP, Wang JXL (2003b) A new north Atlantic oscillation index and its variability. Adv Atmos Sci 20:661–676. https://doi.org/10.1007/BF02915394
Li JP, Swinbank R, Ding RQ, Duan WS (2013) Dynamics and predictability of high-impact weather and climate events. Bull Am Meteorol Soc 94:ES179–ES182. https://doi.org/10.1175/BAMS-D-12-00213.1
Li MT, Gordon AL, Wei J et al (2018) Multi-decadal timeseries of the Indonesian throughflow. Dyn Atmos Oceans 81:84–95. https://doi.org/10.1016/j.dynatmoce.2018.02.001
Li JP, Zheng F, Sun C et al (2019) Pathways of influence of the northern hemisphere mid-high latitudes on east Asian climate: a review. Adv Atmos Sci 36:902–921. https://doi.org/10.1007/s00376-019-8236-5
Li JP, Xie TJ, Tang XX et al (2022) Influence of the NAO on wintertime surface air temperature over east Asia: multidecadal variability and decadal prediction. Adv Atmos Sci 39:625–642. https://doi.org/10.1007/s00376-021-1075-1
Lin RQ, Zheng F, Dong X (2018) ENSO frequency asymmetry and the pacific decadal oscillation in observations and 19 CMIP5 models. Adv Atmos Sci 35:495–506. https://doi.org/10.1007/s00376-017-7133-z
Liu ZY, Di Lorenzo E (2018) Mechanisms and predictability of pacific decadal variability. Curr Clim Change Rep 4:128–144. https://doi.org/10.1007/s40641-018-0090-5
Lorenz EN (1963) Deterministic nonperiodic flow. J Atmos Sci 20:130–141. https://doi.org/10.1175/1520-0469(1963)020%3c0130:DNF%3e2.0.CO;2
Lorenzo ED, Xu T, Zhao Y et al (2023) Modes and mechanisms of pacific decadal-scale variability. Annu Rev Mar Science 15:249–275. https://doi.org/10.1146/annurev-marine-040422-084555
Lou JL, Zheng XG, Frederiksen CS et al (2017) Simulated decadal modes of the NH atmospheric circulation arising from intra-decadal variability, external forcing and slow-decadal climate processes. Clim Dyn 48:2635–2652. https://doi.org/10.1007/s00382-016-3229-x
Ma YW, Li JP, Zhang SQ, Zhao HR (2021) A multi-model study of atmosphere predictability in coupled ocean–atmosphere systems. Clim Dyn 56:3489–3509. https://doi.org/10.1007/s00382-021-05651-w
Mantua NJ, Hare SR, Zhang Y et al (1997) A pacific interdecadal climate oscillation with impacts on salmon production*. Bull Am Meteor Soc 78:1069–1080. https://doi.org/10.1175/1520-0477(1997)078%3c1069:APICOW%3e2.0.CO;2
Meehl GA, Goddard L, Boer G et al (2014) Decadal climate prediction: an update from the trenches. Bull Am Meteorol Soc 95:243–267. https://doi.org/10.1175/BAMS-D-12-00241.1
Meehl GA, Richter JH, Teng HY et al (2021) Initialized earth system prediction from subseasonal to decadal timescales. Nat Rev Earth Environ 2:340–357. https://doi.org/10.1038/s43017-021-00155-x
Msadek R, Dixon KW, Delworth TL, Hurlin W (2010) Assessing the predictability of the Atlantic meridional overturning circulation and associated fingerprints. Geophys Res Lett 37:L19608. https://doi.org/10.1029/2010GL044517
Müller WA, Baehr J, Haak H et al (2012) Forecast skill of multi-year seasonal means in the decadal prediction system of the Max Planck Institute for Meteorology. Geophys Res Lett 39:2012GL053326. https://doi.org/10.1029/2012GL053326
Nan SL, Li JP (2003) The relationship between the summer precipitation in the Yangtze River valley and the boreal spring Southern Hemisphere annular mode. Geophys Res Lett 30:2266. https://doi.org/10.1029/2003GL018381
Newman M, Alexander MA, Ault TR et al (2016) The Pacific decadal oscillation, revisited. J Clim 29:4399–4427. https://doi.org/10.1175/JCLI-D-15-0508.1
Nicolì D, Bellucci A, Ruggieri P et al (2023) The Euro-Mediterranean Center on Climate Change (CMCC) decadal prediction system. Geosci Model Dev 16:179–197. https://doi.org/10.5194/gmd-16-179-2023
Nnamchi HC, Farneti R, Keenlyside NS et al (2023) Pan-Atlantic decadal climate oscillation linked to ocean circulation. Commun Earth Environ 4:121. https://doi.org/10.1038/s43247-023-00781-x
Ogi M, Yamazaki K, Tachibana Y (2004) The summertime annular mode in the Northern Hemisphere and its linkage to the winter mode. J Geophys Res: Atmos 109:2004JD004514. https://doi.org/10.1029/2004JD004514
Pan MT, Zhi XF, Liu ZY et al (2022) Statistical calibrations to improve the 2–5-year prediction skill for SST over the North Atlantic. Meteorol Atmos Phys 134:52. https://doi.org/10.1007/s00703-022-00888-4
Pohlmann H, Botzet M, Latif M et al (2004) Estimating the decadal predictability of a coupled AOGCM. J Clim 17:4463–4472. https://doi.org/10.1175/3209.1
Power S, Tseitkin F, Mehta V et al (1999) Decadal climate variability in Australia during the twentieth century. Int, J Clim 19:169–184. https://doi.org/10.1002/(SICI)1097-0088(199902)19:2%3c169::AID-JOC356%3e3.0.CO;2-Y
Qiu B (2003) Kuroshio extension variability and forcing of the pacific decadal oscillations: responses and potential feedback. J Phys Ocean 33:2465–2482. https://doi.org/10.1175/1520-0485(2003)033%3c2465:KEVAFO%3e2.0.CO;2
Rajagopalan B, Kushnir Y, Tourre YM (1998) Observed decadal midlatitude and tropical Atlantic climate variability. Geophys Res Lett 25:3967–3970. https://doi.org/10.1029/1998GL900065

Rayner NA, Parker DE, Horton EB et al (2003) Global analyses of sea surface temperature, sea ice, and night marine air temperature since the late nineteenth century. J Geophys Res Atmos 108:4407. https://doi.org/10.1029/2002JD002670

Redolat D, Monjo R, Paradinas C et al (2020) Local decadal prediction according to statistical/dynamical approaches. Int J Climatol 40:5671–5687. https://doi.org/10.1002/joc.6543

Ruprich-Robert Y, Moreno-Chamarro E, Levine X et al (2021) Impacts of Atlantic multidecadal variability on the tropical Pacific: a multi-model study. Npj Clim Atmos Sci 4:33. https://doi.org/10.1038/s41612-021-00188-5

Sheffield J, Camargo SJ, Fu R et al (2013) North American climate in CMIP5 experiments. Part II: evaluation of historical simulations of intraseasonal to decadal variability. J Clim 26:9247–9290. https://doi.org/10.1175/JCLI-D-12-00593.1

Smith DM, Scaife AA, Eade R, Knight JR (2016) Seasonal to decadal prediction of the winter North Atlantic Oscillation: emerging capability and future prospects. Q J R Meteorolog Soc 142:611–617. https://doi.org/10.1002/qj.2479

Smith DM, Eade R, Scaife AA et al (2019) Robust skill of decadal climate predictions. Npj Clim Atmos Sci 2:1–10. https://doi.org/10.1038/s41612-019-0071-y

Sun C, Li JP, Jin F-F, Ding RQ (2013) Sea surface temperature interhemispheric dipole and its relation to tropical precipitation. Env Res Lett 8:044006. https://doi.org/10.1088/1748-9326/8/4/044006

Sun C, Li JP, Jin F-F (2015) A delayed oscillator model for the quasi-periodic multidecadal variability of the NAO. Clim Dyn 45:2083–2099. https://doi.org/10.1007/s00382-014-2459-z

Sun C, Kucharski F, Li JP et al (2017) Western tropical Pacific multidecadal variability forced by the Atlantic multidecadal oscillation. Nat Commun 8:15998. https://doi.org/10.1038/ncomms15998

Thompson DWJ, Wallace JM (1998) The Arctic oscillation signature in the wintertime geopotential height and temperature fields. Geophys Res Lett 25:1297–1300. https://doi.org/10.1029/98GL00950

Trenberth KE, Shea DJ (2006) Atlantic hurricanes and natural variability in 2005. Geophys Res Lett 33:L12704. https://doi.org/10.1029/2006GL026894

Vose RS, Huang B, Yin X et al (2021) Implementing full spatial coverage in NOAA's global temperature analysis. Geophys Res Lett 48:e2020GL090873. https://doi.org/10.1029/2020GL090873

Wang H, Kumar A, Wang WQ, Xue Y (2012) Seasonality of the pacific decadal oscillation. J Clim 25:25–38. https://doi.org/10.1175/2011JCLI4092.1

Watanabe T, Yamazaki K (2014) Decadal-scale variation of south Asian summer monsoon onset and its relationship with the pacific decadal oscillation. J Clim 27:5163–5173. https://doi.org/10.1175/JCLI-D-13-00541.1

Wu ZW, Li JP, Wang B, Liu XH (2009) Can the Southern Hemisphere annular mode affect China winter monsoon? J Geophys Res Atmos 114:D11107. https://doi.org/10.1029/2008JD011501

Wu MN, Zhou TJ, Li C et al (2021) A very likely weakening of pacific walker circulation in constrained near-future projections. Nat Commun 12:6502. https://doi.org/10.1038/s41467-021-26693-y

Xie TJ, Li JP, Chen KQ et al (2021) Origin of Indian ocean multidecadal climate variability: role of the north Atlantic oscillation. Clim Dyn 56:3277–3294. https://doi.org/10.1007/s00382-021-05643-w

Xie MM, Wang CZ, Chen S (2022) The role of the maritime continent SST anomalies in maintaining the pacific-japan pattern on decadal time scales. J Clim 35:1079–1095. https://doi.org/10.1175/JCLI-D-21-0555.1

Xue JQ, Li JP, Sun C et al (2018a) Decadal-scale teleconnection between South Atlantic SST and southeast Australia surface air temperature in austral summer. Clim Dyn 50:2687–2703. https://doi.org/10.1007/s00382-017-3764-0

Xue JQ, Sun C, Li JP et al (2018b) Divergent responses of extratropical atmospheric circulation to interhemispheric dipolar SST forcing over the two hemispheres in boreal winter. J Clim 31:7599–7619. https://doi.org/10.1175/JCLI-D-17-0817.1

Xue JQ, Sun C, Li JP, Mao JY (2018c) South atlantic forced multidecadal teleconnection to the midlatitude south Indian ocean. Geophys Res Lett 45:8480–8489. https://doi.org/10.1029/2018GL078990

Yao S-L, Zhou W, Jin F-F, Zheng F (2021) North Atlantic as a trigger for pacific-wide decadal climate change. Geophys Res Lett 48:e2021GL094719. https://doi.org/10.1029/2021GL094719

Yeager S (2020) The abyssal origins of North Atlantic decadal predictability. Clim Dyn 55:2253–2271. https://doi.org/10.1007/s00382-020-05382-4

Yeager SG, Robson JI (2017) Recent progress in understanding and predicting atlantic decadal climate variability. Curr Clim Change Rep 3:112–127. https://doi.org/10.1007/s40641-017-0064-z

Yeager SG, Danabasoglu G, Rosenbloom NA et al (2018) Predicting near-term changes in the earth system: a large ensemble of initialized decadal prediction simulations using the community earth system model. Bull Am Meteor Soc 99:1867–1886. https://doi.org/10.1175/BAMS-D-17-0098.1

Yeager SG, Chang P, Danabasoglu G et al (2023) Reduced Southern Ocean warming enhances global skill and signal-to-noise in an eddy-resolving decadal prediction system. Npj Clim Atmos Sci 6:1–13. https://doi.org/10.1038/s41612-023-00434-y

Zhang R, Delworth TL (2006) Impact of Atlantic multidecadal oscillations on India/Sahel rainfall and Atlantic hurricanes. Geophys Res Lett 33:L17712. https://doi.org/10.1029/2006GL026267

Zhang Y, Wallace JM, Battisti DS (1997) ENSO-like interdecadal variability: 1900–93. J Clim 10:1004–1020. https://doi.org/10.1175/1520-0442(1997)010%3c1004:ELIV%3e2.0.CO;2

Zhang Y, Feng M, Du Y et al (2018) Strengthened Indonesian throughflow drives decadal warming in the southern Indian ocean. Geophys Res Lett 45:6167–6175. https://doi.org/10.1029/2018GL078265

Zhang H-M, Lawrimore J, Huang BY et al (2019a) Updated temperature data give a sharper view of climate trends. Eos. https://doi.org/10.1029/2019EO128229

Zhang R, Sutton R, Danabasoglu G et al (2019b) A review of the role of the Atlantic meridional overturning circulation in Atlantic multidecadal variability and associated climate impacts. Rev Geophys 57:316–375. https://doi.org/10.1029/2019RG000644

Zhang W, Kirtman B, Siqueira L et al (2021) Understanding the signal-to-noise paradox in decadal climate predictability from CMIP5 and an eddying global coupled model. Clim Dyn 56:2895–2913. https://doi.org/10.1007/s00382-020-05621-8

Zhou W, Li JX, Yan ZX et al (2024) Progress and future prospects of decadal prediction and data assimilation: a review. Atmos Oceanic Sci Lett 17:100441. https://doi.org/10.1016/j.aosl.2023.100441